Available online at www.sciencedirect.com

ScienceDirect

Geochimica et Cosmochimica Acta xxx (2022) xxx–xxx

Geochimica et Cosmochimica Acta

www.elsevier.com/locate/gca

Earliest evidence of nebular shock waves recorded in a calcium-aluminum-rich Inclusion

Prajkta Mane [a,b,*], Shawn Wallace [c], Maitrayee Bose [b], Paul Wallace [a,1], Meenakshi Wadhwa [b], Juliane Weber [a,2], Thomas J. Zega [a,d]

[a] *Lunar and Planetary Laboratory, University of Arizona, Tucson, AZ 85721, USA*
[b] *School of Earth and Space Exploration, Arizona State University, Tempe, AZ 87287, USA*
[c] *EDAX, Ametek, Materials Analysis Division, Mahwah 07430, USA*
[d] *Dept. of Materials Science and Engineering, University of Arizona, Tucson 85721, USA*

Received 27 February 2021; accepted in revised form 14 June 2022; available online xxxx

Abstract

Calcium-aluminum-rich inclusions (CAIs) and chondrules are among the most predominant chondritic components contained within primitive meteorites. As CAIs are the first solids to form in the solar nebula, they contain a record of its earliest chemical and physical processes. Here we combine electron backscatter diffraction (EBSD) and ^{26}Al-^{26}Mg chronology techniques to determine the crystallographic properties and ages of CAI components that provide temporal as well as spatial constraints on their origins and subsequent processing in the solar protoplanetary disk. We find evidence of shock deformation within a CAI, suggesting that it was deformed as a free-floating object soon after the CAI formation at the beginning of the Solar System. Our results suggest that even though CAIs and chondrules formed in distinct environments and on different timescales, they were likely affected by similar shock processes that operated over large temporal (0 to ~4 Ma) and spatial (0.2 to at least 2 to 3 au) extents. Our results imply that nebular shock events were active on a wider scale in the solar protoplanetary disk than previously recognized.

Keywords: Early solar system; Nebular shocks; Calcium-aluminum rich inclusions; Electron backscatter diffraction; ^{26}Al-^{26}Mg chronology

1. INTRODUCTION

Calcium-aluminum rich inclusions (CAIs) hosted in chondritic meteorites are the oldest solids to have formed in the Solar System and define its age as 4567.30 ± 0.16 Ma (Amelin et al., 2010; Connelly et al., 2012). Based on short-lived ^{26}Al-^{26}Mg chronology and absolute Pb-Pb chronology, the formation of most CAIs is restricted to within the first ~1 Ma of Solar System history (Connelly et al., 2012; MacPherson et al., 2012, 2017). Therefore, CAIs contain records of the processes active during the earliest period (<1 Ma) of the Solar System. The mineralogy of CAIs is consistent with thermodynamic models that predict the condensation of refractory mineral phases from the solar nebula gas (e.g., Ebel, 2006). The compositional, structural, and isotopic properties of CAIs preserve records of their high-temperature origins and contain evidence of secondary processes that were active during and after their formation, such as aggregation, melting and recrystallization, evaporation, thermal and shock processing, and aqueous alteration in nebular and parent-body settings.

* Corresponding author at: Lunar and Planetary Institute, USRA, Houston, TX 77058, USA.
E-mail address: pmane@lpi.usra.edu (P. Mane).
[1] Current Address: Oregon Physics, Beaverton, OR 97006, USA.
[2] Current Address: Oak Ridge National Laboratory, Oak Ridge, TN 37830, USA.

https://doi.org/10.1016/j.gca.2022.06.006
0016-7037/

In addition to CAIs, chondrules are one of the important petrographic components of chondritic meteorites. Some chondrules formed contemporaneously with CAIs, but a majority of them continued forming for ~4 Ma afterward (Villeneuve et al., 2009; Connelly et al., 2012; Bollard et al., 2017). Thermodynamic properties of CAIs suggest that they formed close to the Sun (<1 au) under reducing conditions (Beckett et al., 1988; Grossman et al., 2008) and inherited an O-isotopic composition close to the solar value (McKeegan et al., 2011). In comparison, chondrules formed under relatively oxidizing conditions (Grossman et al., 2008) and inherited an O-isotopic composition close to that of the terrestrial planets (Yurimoto et al., 2008). Several studies have shown that there exists a chemical complementarity between the compositions of chondrules and the matrix of the host meteorite (Bland et al., 2005; Hezel and Palme, 2008, 2010; Palme et al., 2015). The chemical complementarity between chondrules and the chondritic matrix in which they occur implies that they are cogenetic and formed in the same region, i.e., the chondrite-forming region at ~2 to 3 au (the location of the current asteroid belt), or as some recent models have suggested, perhaps even further beyond Jupiter for carbonaceous chondrites (Kruijer et al., 2017a). Therefore, even though CAIs and chondrules coexist in chondritic meteorites, they formed in distinct nebular environments and over different timescales.

The properties of CAIs and chondrules also suggest distinct origins. Equilibrium thermodynamic models predict the condensation of refractory mineral phases directly from the solar nebular gas, such as those contained within CAIs (Ebel, 2006). In contrast, chondrules, molten silicate droplets within the solar nebula, are not predicted to form in the protoplanetary disk by such models (Connolly and Jones, 2016). The mineralogical, chemical, and isotopic compositions of chondrules indicate that they were flash heated in the solar protoplanetary disk, likely in a region with an enhanced dust-to-gas ratio that was distinct from the CAI-forming region. Chondrules were heated to peak temperatures of ~1750 to 2370 K and then cooled quickly (~10^3 – 10^4 K/h) above the liquidus and slowly (~250 K/h) below the liquidus (Desch et al., 2012 and references therein).

Chondrules formed by the melting of solid precursors in dust-rich regions of the protoplanetary disk during transient heating events. However, early Solar System processes that could have led to the melting of solid precursor materials and hence the formation of chondrules in the solar protoplanetary disk remain poorly understood. Various mechanisms proposed to explain chondrule formation include shock waves in early protoplanetary disk, nebular lightening, impact plumes generated during planetary collisions, radiative heating of dust clumps, and magnetic current sheets (Connolly and Jones, 2016). It is likely that more than one such mechanism was responsible for the melting of chondrules found in different primitive meteorites. One of the chondrule formation mechanisms that has received considerable attention is rapid heating by a shock wave, through either gravitational instability driven shock (Hood and Horanyi, 1991; Wood, 1996) or planetesimal bow shock (Hood, 1998; Weidenschilling et al., 1998). Further, multiple shock waves, weaker than those responsible for the melting of chondrules, were proposed as a mechanism that compacted the fine-grained rims around chondrules (Bland et al., 2011). Similarly, electron back scatter diffraction (EBSD) and transmission electron microscope (TEM) analysis of some chondrules reveal that they record deformation features as a result of either nebular shocks or impacts on the meteorite parent bodies (Forman et al., 2016; Zolensky et al., 2020). In addition to chondrules, certain types of CAIs, i.e., igneous type-B CAIs, were also reheated and melted, possibly by mechanisms related to those responsible for chondrule formation (Richter et al., 2006). However, in either case, whether chondrules or CAIs, the presence of such shocks remains to be verified by astrophysical observations of extrasolar protoplanetary disks, and if they did occur within our solar nebula, there are few quantitative constraints on their spatial and temporal extent. Here, we report microstructural analysis of a CAI that preserves evidence of shock deformation, and we constrain the timescale of this deformation event by ^{26}Al-^{26}Mg analyses of the CAI components.

2. SAMPLES AND METHODS

2.1. Sample preparation

Northwest Africa (NWA) 5028 is a CR2.6 carbonaceous chondrite with a weathering grade W1 and shock grade S2 (Harju et al., 2014). The meteorite sample containing the CAI designated as 'Hedgehog' was acquired from the Center for Meteorite Studies at Arizona State University (ASU). This CAI is named after the hedgehog cactus found in Arizona where it was identified, and the majority of the analytical work was done. The meteorite fragment was sliced and mounted in a 1-inch epoxy disk. It was ground smooth using successive SiC pads of 600, 800, and 1200 grits with water for lubrication. These grinding steps were followed by a sequence of polishing steps using diamond paste with particle sizes of 3, 1, and 0.25 μm for ~5 mins each. Once polished, the section was coated with a ~15 nm thick carbon coat for electron microprobe analysis.

For EBSD analysis, a flat sample surface and a thin carbon coat are essential requirements. Therefore, after the electron microprobe analysis, the sample was additionally polished on a Pace® Technologies vibratory polisher on a synthetic rayon all-purpose cloth with 0.05 μm colloidal silica (pH 9.8) for ~2 h. The sample was then cleaned using water in an ultrasonicator for 10 mins. The sample was dried and coated with a ~2 nm thick carbon layer using a Leica ACE600 carbon coater prior to EBSD analysis.

2.2. Electron microprobe analysis

Petrographic characterization of Hedgehog was performed using electron microprobe analysis (EMPA). Backscattered electron (BSE) images and elemental X-ray maps were acquired with the JEOL JXA-8530F electron microprobe at ASU. The detailed X-ray maps were made at 1 μm/pixel resolution. The major element abundances

Please cite this article in press as: Mane P., et al. Earliest evidence of nebular shock waves recorded in a calcium-aluminum-rich Inclusion. *Geochim. Cosmochim. Acta* (2022), https://doi.org/10.1016/j.gca.2022.06.006

of minerals were determined using wavelength dispersive spectroscopy (WDS) spot analyses using a Cameca SX 100 electron microprobe at the Kuiper Materials Imaging and Characterization Facility (KMICF) in the Lunar and Planetary Laboratory (LPL) University of Arizona (UA). The electron probe was operated at 15 kV and with a beam current of 20 nA, and equal peak and background counting times of 20 s per element. Various terrestrial mineral standards were used for calibration of elemental abundances as follows: Mg and Si: olivine (Fo_{92}); Na: albite; Ca and Al: anorthite; Fe: fayalite; K: orthoclase; Cr: chromite; Ti: rutile; and Mn: rhodonite. Typical detection limits were 0.05% for oxide abundances.

2.3. EBSD analysis

Selected areas of Hedgehog were mapped using the ThermoFisher Helios 660 focused-ion-beam scanning electron microscope (FIB-SEM) at KMICF (LPL, UA). The SEM is equipped with EDAX Octane Plus EDS and Hikari XP EBSD detectors enabling automated simultaneous EDS and EBSD mapping. For EBSD, the SEM was operated at 20 keV accelerating voltage and 6.4 nA beam current. The sample was tilted at 70° toward the EBSD detector and was mapped on a hexagonal grid with a fixed step of 0.2 μm to ensure that each grain contained several pixels. The use of a hexagonal grid provides a constant point-to-point distance to all neighboring pixels, which compared to a square grid, minimizes the artifacts in the determination of grain boundaries, grain shapes, and statistical analyses of triple junctions. The EDS and EBSD data were collected and processed using TEAM™ and OIM Analysis 8™ software, enabling the construction of EBSD maps and calculation of EBSD parameters. All EBSD patterns were saved for post-collection data processing. We mapped nine regions of Hedgehog (shown as yellow boxes in Fig. 1 as maps a, b, c, d, e, f, g, h, and i) totaling >40 h of analysis time. The EBSD analysis was conducted on ~5% of the total CAI area, which may not be representative of the entire CAI and may introduce selection bias. However, we selected areas that contained both the rim and the interior (maps a, b, c, f, i) from different regions of Hedgehog to ensure that the microstructural observations are obtained from all over the inclusion and not limited to one region of the CAI. Additionally, we selected area 'a' because it contains overlapping rims region, area 'b' as it contains spinel palisade structure, and area 'g' as it samples WL rims exclusively. We also analyzed area 'd', interior to area 'c', to evaluate whether the microstructures change towards the center of the inclusion. Area 'i' was selected because of the deformed chondrule (based on its shape) adjacent to the CAI. While selecting the regions for EBSD data collection, we avoided fine-grained alteration and regions that showed significant topography including pits and cavities (e.g., the spinel-rich core of the CAI that shows significant topography and surface relief), because EBSD data quality is sensitive to surface topography.

The Kikuchi diffraction patterns generated by EBSD, also called electron backscatter patterns (EBSP), were indexed using a triplet indexing technique and neighbor

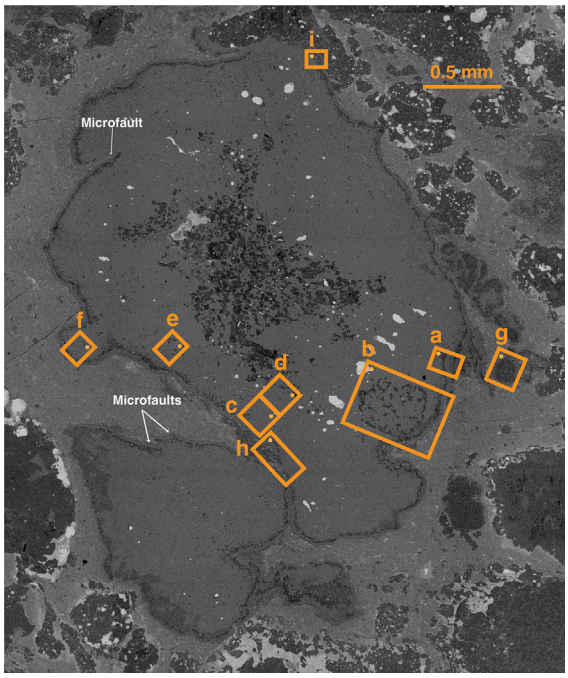

Fig. 1. BSE image of Hedgehog. The orange boxes show regions where EDS and EBSD data were collected. The orange dots in each box show the top right orientation of the EDS-EBSD maps shown in Figs. 4–6 and S1-S7, Arrows indicate locations of microfaults.

pattern averaging with re-indexing (NPAR) described in Wright et al. (2015). The EBSD patterns for melilite and spinel were indexed based on crystallographic data files downloaded from the American Mineralogist Database for melilite (a = 7.74 Å; c = 4.932 Å; Merlini et al., 2009), and spinel (a_0 = 8.084 Å; Peterson et al., 1991). We used the post-acquisition cleaning routine in the OIM Analysis 8™ software based on grain confidence index (CI) standardization and partitioning out pixels with CI < 0.1 as described in Field (1997). Criteria for grain identification were set at a minimum of 10 contiguous pixels and a grain tolerance angle of 12 to 15°. The grain tolerance angle for the individual map was defined based on the unique grain map showing reasonable grain boundaries. The grain size of the pyroxene layer in the WL rims is too small to index successfully using these criteria and define a grain, and so there is no EBSD data presented for pyroxene in this work. Thus, the data for melilite and spinel were used to determine deformation parameters. For each mapped region, inverse pole figure (IPF) maps were constructed. For each mineral grain, the effective grain size, defined as the diameter of a circular grain with the same area as measured, and two deformation metrics were calculated: 1) Grain Orientation Spread (GOS), representing average deviation in orientation between each point in a grain and the average orientation of the grain (Brewer et al., 2009; Wright et al., 2011); and 2) Grain Average Misorientation (GAM), representing the average misorientation between each neighboring pairs of measurement points within the grain (Wright et al., 2011). Similarly, for each region, the following maps were created: 1) Kernel

Please cite this article in press as: Mane P., et al. Earliest evidence of nebular shock waves recorded in a calcium-aluminum-rich Inclusion. *Geochim. Cosmochim. Acta* (2022), https://doi.org/10.1016/j.gca.2022.06.006

Average Misorientation (KAM), representing the mean misorientation between a central pixel from its surrounding six neighbors; and 2) Grain Reference Orientation Deviation Angle (GROD angle) representing the mean misorientation of each pixel from a reference, mean orientation of the grain. The analytical precision for crystallographic orientation was estimated to be ~0.2° by analyzing a single crystal silicon sample for a KAM map to evaluate the spread in the orientation as described in Wright et al. (2014). The mean angular deviation values range from 1.2 to 1.6° for these maps.

2.4. ^{26}Al-^{26}Mg chronology using NanoSIMS

Magnesium isotopic ratios and ^{27}Al/^{24}Mg ratios were measured in the secondary ion mass spectrometry (SIMS) lab at ASU. We used the Cameca NanoSIMS 50L over two analytical sessions with protocols similar to those described previously (Ito and Messenger, 2010). The thick section of NWA 5028 containing Hedgehog was gold-coated and sputtered by a 16 keV primary O^- beam with a current of ~20 to 50 pA. The primary beam was rastered over 5 × 5 μm areas on the sample and each spot was pre-sputtered with a higher current (~100 pA) until the secondary counts were stabilized (~3–5 mins) to remove the conductive carbon coating and to achieve sputtering equilibrium. Positive secondary ions were collected from the central 2.5 × 2.5 μm area by using electronic gating. Positive secondary ions of $^{24}Mg^+$, $^{25}Mg^+$, $^{26}Mg^+$, and $^{27}Al^+$ were collected simultaneously using electron multipliers (EM) in isotope ratio mode. Potential isobaric interferences were resolved using a mass resolving power (MRP) of >9000 based on the Cameca definition where MRP = (1/4) × (r/L) where r is the radius of the magnet and L is the width of the portion of the mass peak between 10% and 90% of the maximum intensity, a measure for the steepness of the peak flanks (Hoppe et al., 2013). We used the NMR (Nuclear Magnetic Resonance) tool to regulate magnetic field stability; within a session, the variation in the magnetic field was <10 ppm.

The Mg isotopic ratios (^{25}Mg/^{24}Mg and ^{26}Mg/^{24}Mg) were corrected for dead time. The instrumental mass bias was corrected using the following natural and synthetic terrestrial standards: San Carlos olivine, Madagascar Hibonite, two terrestrial melilites, and synthetic NIST SRM 610 glass. Analysis time varied between 10 and 30 min per spot for different mineral phases to optimize the total counts of the secondary ions.

The instrumental mass fractionation (IMF) is defined as

$$\alpha_{25,26} = \frac{(^{25,26}Mg/^{24}Mg)_m}{(^{25,26}Mg/^{24}Mg)_{true}}$$

where "m" denotes the measured ratio and "true" ratios are the Mg isotopic ratios $(^{25}Mg/^{24}Mg)_{ref}$ = 0.12663 and $(^{26}Mg/^{24}Mg)_{ref}$ = 0.13932 (Catanzaro et al., 1966). The IMF follows the following exponential mass fractionation relationship.

$\alpha_{25} = (\alpha_{26})^{\beta}$The quantity β is the IMF factor of 0.5128 (Davis et al., 2015).

$$\delta^{25,26}Mg' = ln\alpha_{25,26} \times 1000$$

The radiogenic excess in ^{26}Mg is then calculated as

$$\delta^{26}Mg^* = \delta^{26}Mg - \left[\left(1 + \frac{\delta^{25}Mg}{1000}\right)^{\frac{1}{\beta}} - 1\right] \times 1000$$

The long-term external reproducibility (2σ) based on repeat analyses of terrestrial standards with different ^{27}Al/^{24}Mg ratios calculated over two analytical sessions, each lasting 1 to 2 weeks (see below) are as follows: San Carlos olivine δ^{26}Mg* = ±3.2‰; terrestrial melilite-1 δ^{26}Mg* = ±2.8‰; terrestrial melilite-2 δ^{26}Mg* = ±2.0‰; NIST SRM 610 δ^{26}Mg* = ±12.9‰; Madagascar hibonite δ^{26}Mg* = ±6.04‰.

The ^{27}Al/^{24}Mg (atomic) ratios of the unknown samples were determined using terrestrial standards. These include: San Carlos olivine (^{27}Al/^{24}Mg = 0.0006); terrestrial melilite-1 (^{27}Al/^{24}Mg = 0.65); terrestrial melilite-2 (^{27}Al/^{24}Mg = 28.4); and Madagascar hibonite (^{27}Al/^{24}Mg = 27.9). The relative sensitivity factor (RSF) for each standard was calculated by comparing the true ^{27}Al/^{24}Mg ratio with the ^{27}Al/^{24}Mg ratios measured using NanoSIMS:

$$RSF = \frac{\left(\frac{^{27}Al}{^{24}Mg}\right)_{true}}{\left(\frac{^{27}Al}{^{24}Mg}\right)_{measured}}$$

This RSF value was then used to calculate the true ^{27}Al/^{24}Mg ratio of unknown samples:

$$\left(\frac{^{27}Al}{^{24}Mg}\right)_{true} = RSF \times \left(\frac{^{27}Al}{^{24}Mg}\right)_{measured}$$

The uncertainties for the Mg isotopic compositions (2σ) are.

$$\sigma_{final} = \sqrt{\sigma^2_{internal} + \sigma^2_{external}}$$

where $\sigma_{internal}$ is the standard error of the mean of the δ^{26}Mg* of each unknown and $\sigma_{external}$ is the standard error of the mean of repeated measurements of the terrestrial standards. The uncertainties for ^{27}Al/^{24}Mg ratios are calculated based on the percentage reproducibility (2σ) of repeated analyses of the terrestrial standards with the most similar ^{27}Al/^{24}Mg ratios. We used IsoPlotR to calculate the slopes, intercepts, and mean squared weighted deviations (MSWDs) for both the isochrons (Vermeesch, 2018).

2.5. Focused-ion-beam scanning-electron microscopy

We used a ThermoFisher Helios 660 dual beam FIB-SEM at the KMICF (LPL, UA) to make an electron-transparent section (~100 nm) of a spinel-melilite interface from the interior of Hedgehog. We used the *in-situ* techniques previously described (Zega et al., 2007), except that the section was extracted with a W needle and welded to a Cu half grid in flagpole-style geometry. The section was thinned with Ga^+ at 30 keV and 0.23 nA down to a thickness of ~100 nm after which the voltage was lowered progressively to 16, 8, and 5 keV and varied currents from 0.2 nA to 80 pA to polish off the damage layer created by higher voltage milling.

2.6. Transmission electron microscopy

We examined the FIB section using a 200 keV Hitachi HF5000 scanning transmission electron microscope (S/TEM) in KMICF (LPL, UA). The HF5000 is equipped with a cold-field-emission gun, a 3rd-order spherical aberration-corrector for STEM imaging, and bright-field (BF) and dark-field (DF) STEM detectors. The HF5000 is also equipped with an Oxford Instruments X-max side-entry energy-dispersive spectrometer (EDS) system that includes dual 100 mm^2 silicon-drift detectors (SDD) providing a ~2 sr solid angle of collection. The chemical composition of the FIB section was determined qualitatively using spectrum imaging. The spectrum images were acquired using a 20 keV energy range dispersed over 2048 channels, a mapping resolution of 512 × 512 px, a process time of 5, a pixel dwell time of 25 µs, and a pixel size of 20 nm. Selected-area electron-diffraction (SAED) patterns were acquired for multiple grains to determine their phase and crystallographic orientation. All patterns were acquired with a Gatan OneView CMOS camera and measured based on calibrated camera constants. All the SAED patterns were indexed both manually (measured in Photoshop) and using the crystallographic image processing software package, CRISP (Hovmöller, 1992). Oriented DF and BF images of individual melilite and spinel grains were acquired to determine whether they contain dislocations.

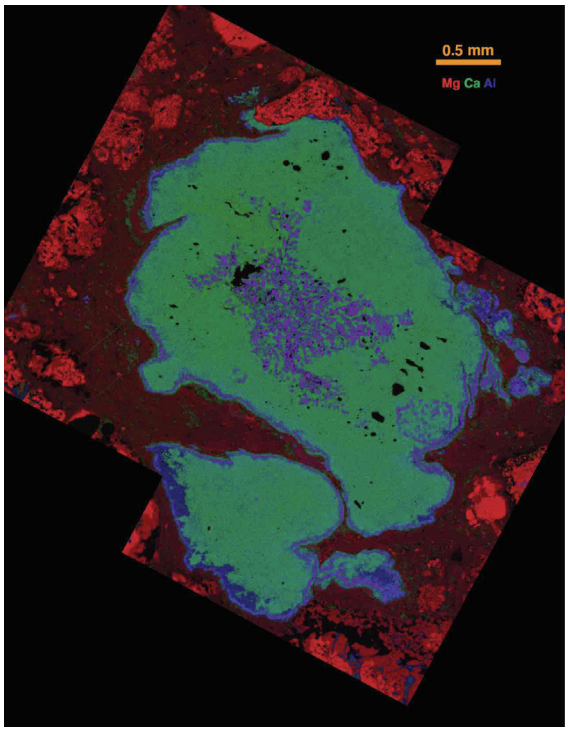

Fig. 2. X-ray false color composite map of Hedgehog showing Mg in red, Ca in green, and Al in blue. In this map, melilite is shown as green and, spinel is shown as magenta. Nepheline occurs as an alteration phase close to the WL rims and is shown in blue.

3. RESULTS

3.1. Petrography and mineralogy

Hedgehog is elongated, ~2.9 mm × ~1.6 mm in size, and contains melilite and spinel as major mineral phases. It contains minor perovskite and also hosts opaque mineral assemblages (Figs. 1, 2, 3). These characteristics, combined with its morphology, classify Hedgehog as a type-A CAI (Grossman, 1975, 1980). Hedgehog is surrounded by a ~70 µm thick Wark-Lovering (WL) rim (Wark and Lovering, 1977), which is a sequence of multi-mineralic layers. These WL rims consist of an innermost hibonite, perovskite, and spinel layer, followed by a middle melilite layer, and an outermost pyroxene layer (Fig. 3a, b). Next to Hedgehog is a heart-shaped CAI (~1.3 × 0.9 mm), with similar mineralogy and also surrounded by a WL rim sequence (Figs. 1, 3c). These two CAIs are likely part of the same inclusion that is connected in the third dimension.

The interior melilite occurs as an interlocking mass of blocky or lath-shaped crystals as seen in the IPF maps (Figs. 4b, 5b, S1b-S7b). The åkermanite content in melilite varies from Åk7 to Åk38 (n = 16, see Table S1). Some individual melilite grains show reverse zoning, similar to those seen in many fluffy type-A CAIs (Grossman, 1980) (Fig. 6). In some regions of Hedgehog, melilite is more gehlenitic in composition close to the WL rims (Fig. 6a, c), whereas other regions near the WL rims do not show this zoning (Fig. 6b, f). Most melilite grains poikilitically enclose spinel (Fig. 3a, b). Spinel grains are small (1–25 µm) with subhedral morphologies and form clusters that are concentrated in the center of the CAI but occur sparsely in the outer region of the inclusion (Fig. 1). Some spinel grains are arranged in a shell-like structure (Fig. 3b), similar to those described as spinel palisade bodies, commonly found in compact type-A and type-B CAIs that have experienced melting (El Goresy et al., 1979; Simon and Grossman, 1997). The presence of reverse zoning in some melilite and spinel palisade structures suggests that Hedgehog is transitional between fluffy and compact type-A CAIs and has not experienced complete melting. Spinel grains are homogeneous and near-end member $MgAl_2O_4$ (Table S1) but contain minor TiO_2 (0.3–0.5 wt%) and Cr_2O_3 (0.1–0.4 wt%). Perovskite occurs as mostly isolated subhedral to anhedral grains enclosed in melilite and can occur in contact with spinel. Perovskites are near-endmember $CaTiO_3$ with minor SiO_2, Al_2O_3, and FeO (Table S1). The opaque mineral assemblages contain Fe-Ni rich metal grains (Fig. 3d) that show compositional zoning. Hedgehog contains Fe-Ni metal grains and negligible FeO in its silicate phases. Some of the metal grains host Fe-oxide inclusions that contain Cr and V. These metal assemblages have Fe-oxide and phosphate layers around them (Fig. S8).

The innermost layer of the WL rim contains spinel, hibonite, and perovskite grains (Fig. 3e, f). Hibonite in the WL rim contains 2.1 to 3.4 wt% MgO, 4.2 to 6.8 wt% TiO_2, and minor (0.1 to 0.5 wt%) FeO (Table S1). Similar to the interior, WL rim spinel grains are homogeneous and near endmember $MgAl_2O_4$. They contain trace TiO_2 (0.3 wt%), Cr_2O_3 (0.1 wt%), CaO (~0.1 to 0.2 wt%), and

Please cite this article in press as: Mane P., et al. Earliest evidence of nebular shock waves recorded in a calcium-aluminum-rich Inclusion. *Geochim. Cosmochim. Acta* (2022), https://doi.org/10.1016/j.gca.2022.06.006

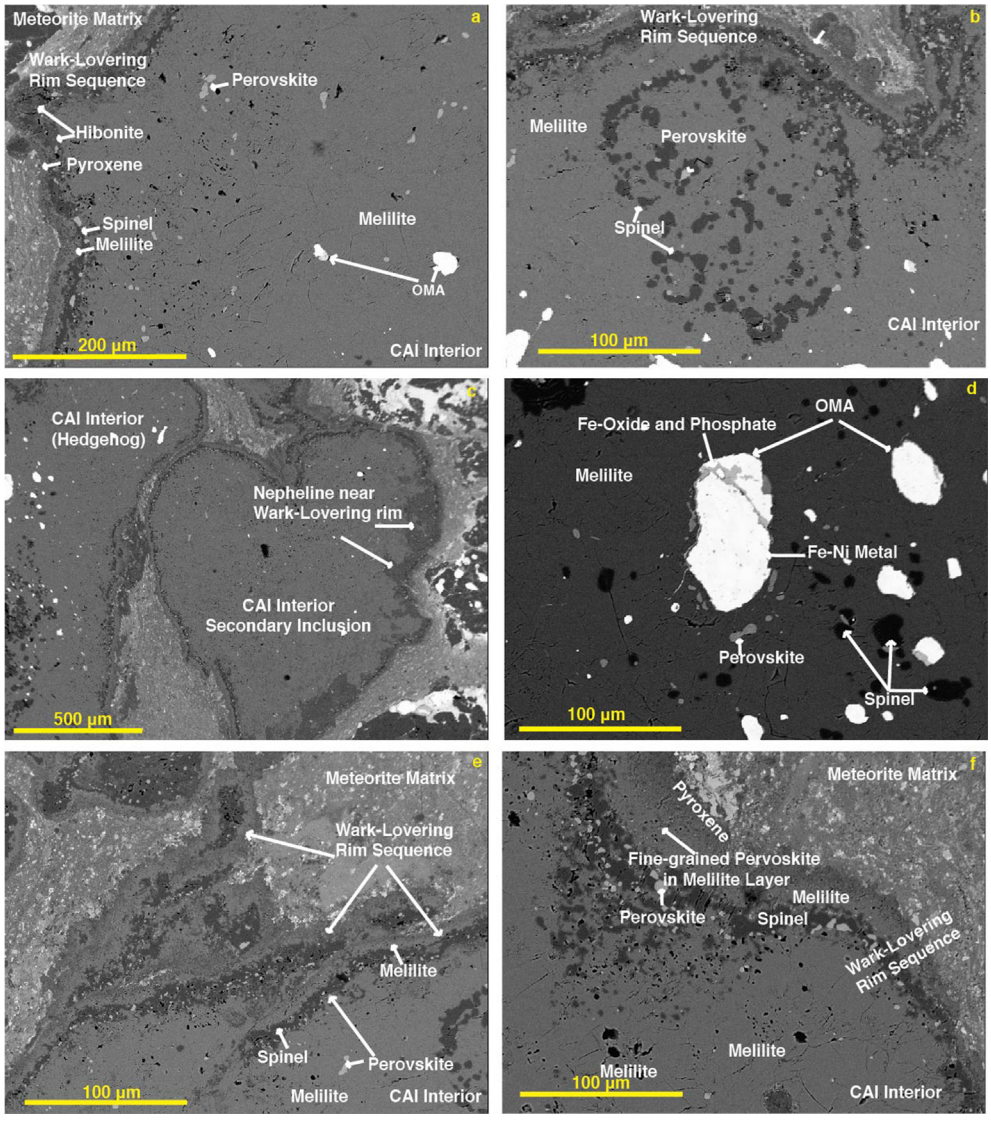

Fig. 3. BSE images of different regions of Hedgehog. (a) The interior as well as a portion of the WL rim showing major mineral phases in Hedgehog. (b) Spinel palisade structure in Hedgehog. (c) The secondary inclusion adjacent to Hedgehog, with similar mineralogy. (d) Opaque metal assemblages in Hedgehog. (e) Overlapping WL rim sequence. (f) WL rim sequence of Hedgehog showing smaller perovskite grains in the middle melilite layer.

FeO (0.1 to 0.5 wt%). Perovskites are near endmember $CaTiO_3$ with minor SiO_2, Al_2O_3, and FeO. The intermediate layer contains coarse-grained melilite (grain size ~1 to 17 µm) with smaller perovskite grains dispersed in it (Fig. 3f). The WL rim melilite is Al-rich, with åkermanite content varying from Åk9 to Åk16. The WL-rim melilite also contains minor FeO (0.1 to 0.6 wt%), and minor TiO_2 (~0.1 wt%). The outermost layer contains fine-grained Ti-rich pyroxene (grain size <1 µm). The rim melilite shows triple junctions (Figs. 4b, and 5b), suggesting annealing after the formation of the rims. In some regions, these layers are repeated, overlapping with each other (Fig. 3e). These apparent multiple layers could be due to an observational bias of looking at a complex three-dimensional object in a two-dimensional section. The WL rims show the presence of microfaults (Fig. 1).

3.2. Microstructural analysis using EBSD

We mapped the crystallographic orientation and chemical composition of several regions of Hedgehog using EBSD and EDS (Figs. 4–6, S1-S7). Fig. 4 shows EBSD data for the region of Hedgehog that contains melilite and spinel in the interior of the CAI, including the spinel palisade structure and spinel and melilite in a segment of its WL rims. Fig. 5 shows EBSD data for the region of Hedgehog with the overlapping WL rim sequence. Figs. S1-S7 show EBSD data for melilite and spinel for different regions of Hedgehog's interior and WL rims. Fig. S6 shows EBSD data specifically for the WL rim region. Fig. S7 shows EBSD data for the adjacent chondrule, in addition to EBSD data for interior melilite and WL rim melilite and spinel. The deformation in melilite and some spinel grains

Please cite this article in press as: Mane P., et al. Earliest evidence of nebular shock waves recorded in a calcium-aluminum-rich Inclusion. *Geochim. Cosmochim. Acta* (2022), https://doi.org/10.1016/j.gca.2022.06.006

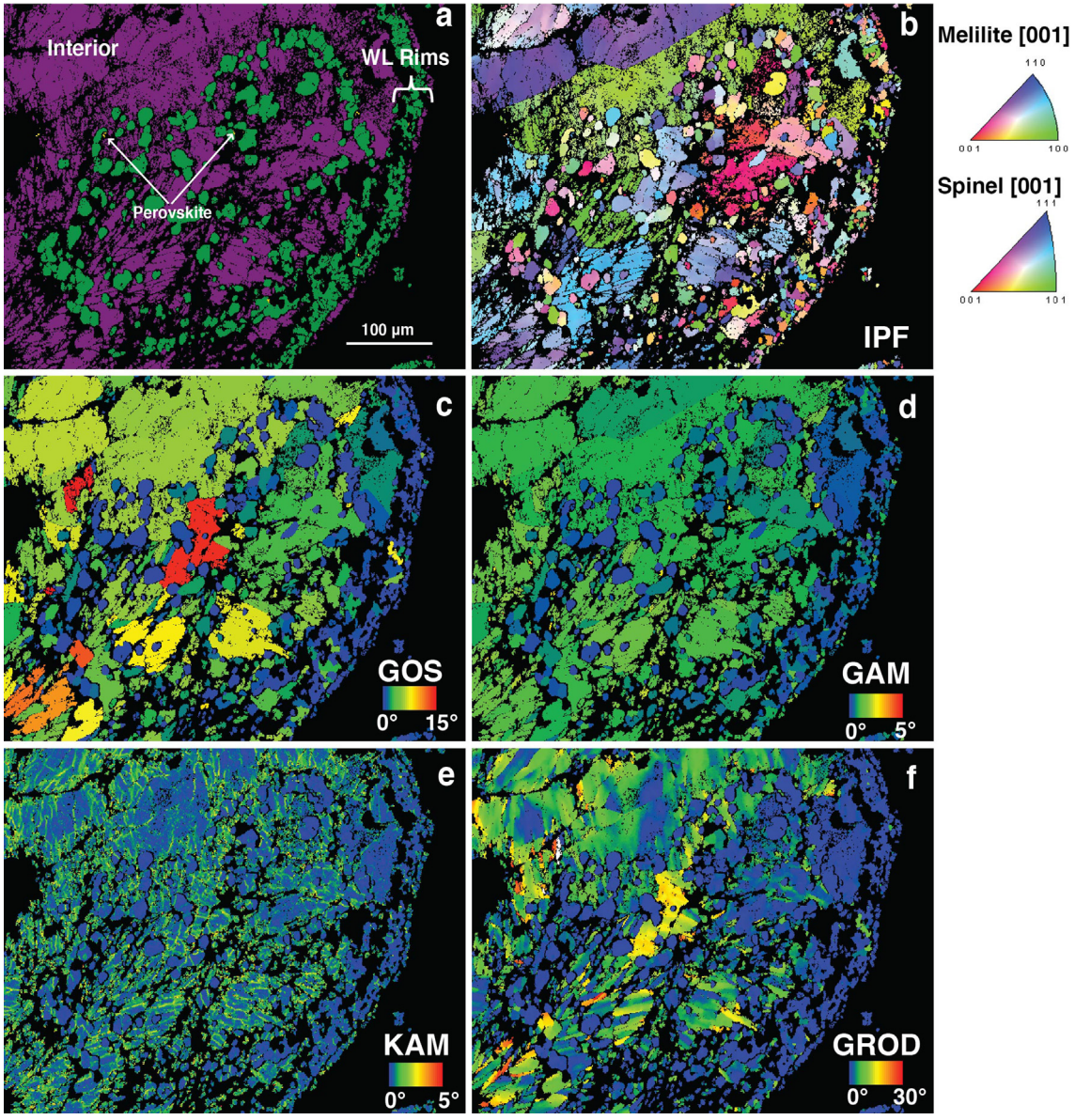

Fig. 4. EBSD data for region 'b' in Hedgehog as shown in Fig. 1. The map contains interior as well as rim spinel and melilite. (a) Phase map of the region showing melilite in purple and spinel in green. The Wark-Lovering rim sequence contains an innermost layer of spinel (in green) + perovskite (yellow) and a middle melilite layer (purple). (b) Inverse pole figure (IPF) map of melilite and spinel. (c) Grain orientation spread (GOS) map. (d) Grain average misorientation (GAM) map of the region. (e) Kernel average misorientation (KAM) map of the region. (f) Grain reference orientation deviation angle (GROD angle) map of the region.

in Hedgehog can be seen as color variations in the IPF maps (Figs. 4–5, S1-S7) and high mean GOS, and GAM values (Tables 1, 2). The KAM maps show that some defects are concentrated near low-angle grain boundaries (Figs. 4e and 5e). Compared to GOS, which highlights the deformation on a grain scale, KAM highlights deformation on a pixel scale. The interior melilite shows variation in the KAM values where higher KAM values are concentrated along the sub-grain boundaries. The GROD angle is a useful parameter to visualize intragrain deformation. As seen in the GROD angle maps (Figs. 4f and 5f), the interior melilite grains show significant variation in the GROD angle parameter compared to the rim melilite. However, only a few spinel grains from the interior and the rim show any variation in the GROD angle. We did not observe any preferred orientation in melilite and spinel or crystallographic orientation relationships between spinel and melilite. The interior melilite shows grain sizes ranging from 0.7 to 140 µm with an average of 2.8 µm, whereas rim melilite grain size ranges from 0.7 to 16.6 µm with an average of 3.4 µm. The variation in grain size is less pronounced in the spinel, where the interior spinel grain size ranges from 0.7 to 25.6 µm with an average grain size of 6.3 µm, and the rim spinel grain size ranges from 0.7 to 18.3 µm with an average

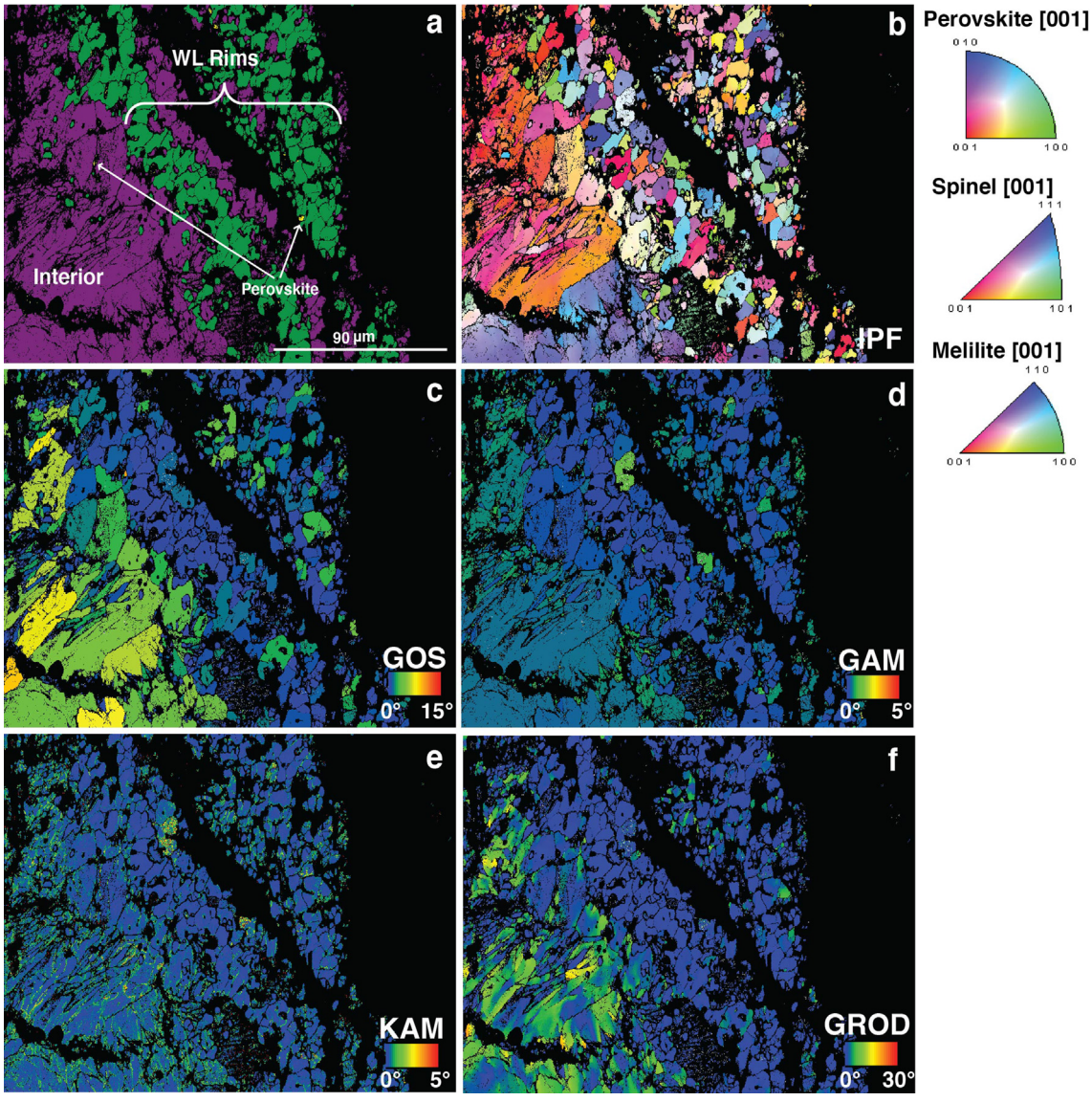

Fig. 5. EBSD data for region 'a' in Hedgehog. The map contains interior as well as rim spinel, perovskite and melilite. (a) Phase map of the region showing melilite in purple, spinel in green, and perovskite in yellow. (b) Inverse pole figure (IPF) map of melilite and spinel. (c) Grain orientation spread (GOS) map. (d) Grain average misorientation (GAM) map of the region. (e) Kernel average misorientation (KAM) map of the region. (f) Grain reference orientation deviation angle (GROD angle) map of the region.

grain size of 4.3 μm. The mean GOS value for interior melilite (1.96) is higher than the rim melilite (1.17). The mean GAM value for interior melilite (0.90) is higher than that of the rim melilite (0.68). The mean GOS value of the interior spinel (1.19) is also higher than the rim spinel (1.14). The mean GAM value for the interior spinel (0.52) is, however, identical to that of the rim spinel (0.52). The frequency distribution of GOS and GAM values of interior and rim melilite, shown in Fig. 7a, b, suggests that the interior melilite records higher GOS and GAM values compared to the rim melilite. The frequency distribution of GOS and GAM values of interior and rim spinel shown in Fig. 7c, d also suggests that interior spinel values are greater than rim spinel values, consistent with melilite but less pronounced. Additionally, Table S1 reports the mean, median, and range of grain size, GOS, and GAM values for both interior and rim minerals (melilite and spinel) for individual maps. Melilite shows large variations in GOS and GAM values (GOS ranging from 0.2 to 13.9 and GAM ranging from 0.2 to 3.9), however, three maps that contain both interior and rim melilite show distinct differences in the frequency distribution of their GOS values (Figs. S9a, b, c), where rim melilite records consistently lower GOS values compared to the interior melilite.

We used a two-sample z-test (Sprinthall and Fisk, 1990) to evaluate if there is a statistically significant difference between the GOS and GAM values for interior and rim mineral grains and assess whether the interior minerals experienced a higher degree of deformation. The two-sample z-test is used to compare the means (GOS and GAM values)

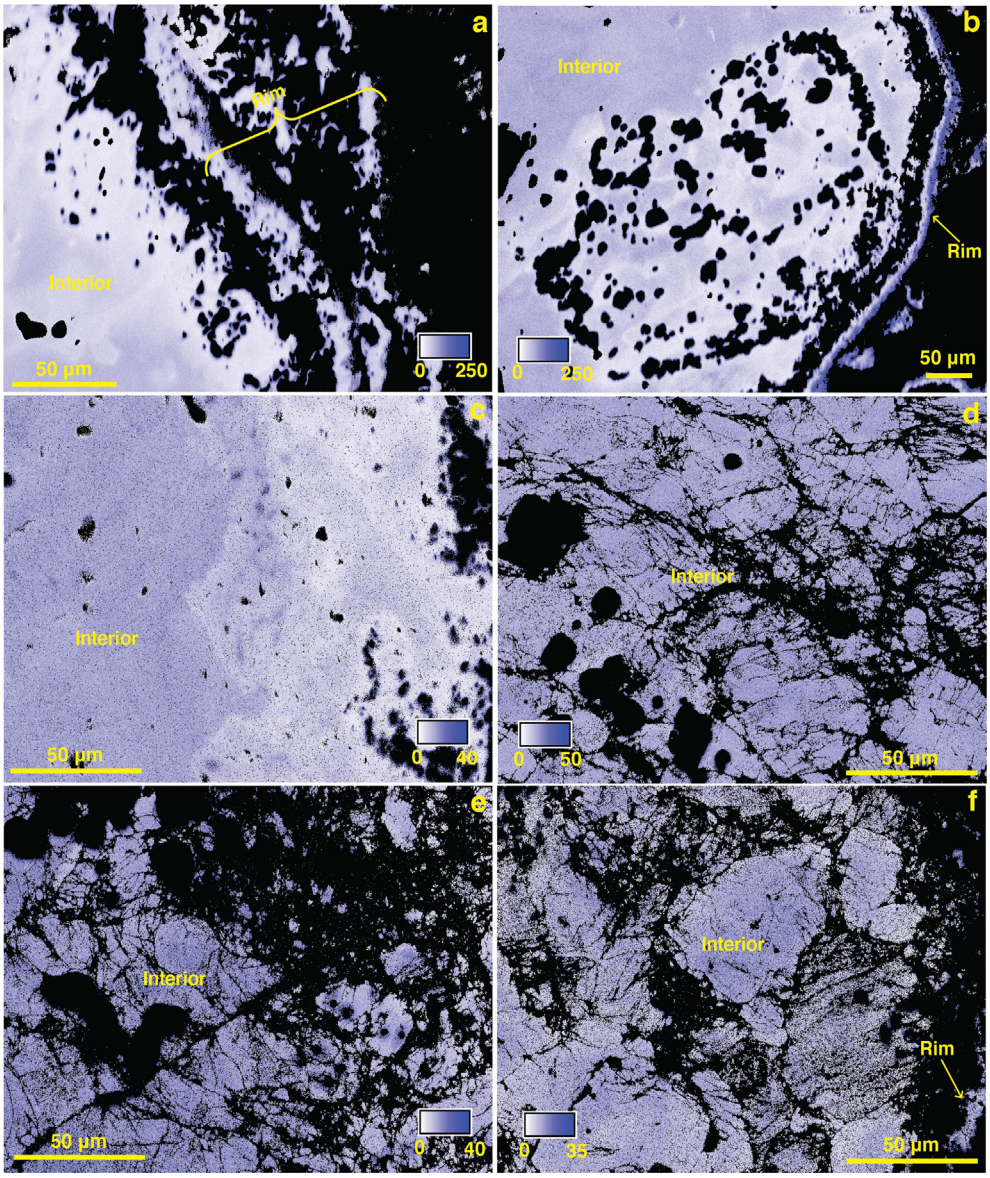

Fig. 6. EDS maps of Mg of Hedgehog highlighting compositional zoning in melilite. (a), (b), (c), (d), (e), and (f) show Mg maps of the region a, b, c, d, e, and f, shown in Fig. 1 in orange boxes, respectively. Spinel in Hedgehog is a pure endmember $MgAl_2O_4$, therefore, it does not show variation in its Mg content. To highlight the Mg zoning in melilite, the range of EDS counts is adjusted so that the spinel grains are blanked out (black). These regions were also analyzed using EBSD. The units are counts of Mg per pixel.

of two independent populations (interior and rim minerals), where the sample size is large ($n > 30$). In the case of interior and rim melilite grains, the probability (P) of the GOS and GAM values having the same mean is <0.01 (Tables 3a, b). Therefore, the interior melilite records more intense deformation compared to the rim melilite, as seen in their GOS and GAM values. The mean GOS values for theweb interior spinel are higher than for the rim spinel. However, applying the z-test revealed that this difference is not statistically significant, i.e., the probability of interior spinel GOS and rim spinel GOS values having the same mean is 0.5 and the probability of interior spinel GAM and rim spinel GAM values having the same mean is 0.8 (Tables 4a, b).

3.3. ^{26}Al-^{26}Mg chronology

We performed ^{26}Al-^{26}Mg dating of the Hedgehog interior and its WL rim using NanoSIMS, to provide time constraints on the deformation episodes (Fig. 8; Table 5). The interior of the CAI defines an isochron with a $^{26}Al/^{27}Al$ ratio of $(6.1 \pm 1.8) \times 10^{-5}$ (2σ) and an initial $\delta^{26}Mg^*$or $(\delta^{26}Mg^*)_0$ of -1.4 ± 2.0‰ (2σ) (MSWD = 1.2). In comparison, the rim defines an isochron with a $^{26}Al/^{27}Al$ ratio of $(6.7 \pm 1.6) \times 10^{-5}$ (2σ) and with $(\delta^{26}Mg^*)_0$ of -1.6 ± 1.6 ‰ (2σ) (MSWD = 1.0). Therefore, both the interior and WL rim phase in Hedgehog record a canonical $^{26}Al/^{27}Al$ ratio within analytical error.

Please cite this article in press as: Mane P., et al. Earliest evidence of nebular shock waves recorded in a calcium-aluminum-rich Inclusion. *Geochim. Cosmochim. Acta* (2022), https://doi.org/10.1016/j.gca.2022.06.006

Table 1
Grain size, GOS, and GAM values for individual EBSD maps shown in Fig. 1.

Map	*Interior Melilite (Grainsize μm)*			*Rim Melilite (Grain size μm)*			*Interior Spinel (Grain size μm)*			*Rim Spinel (Grain size μm)*		
	Mean	Median	Range	Mean	Median	Range	Mean	Median	Range	Mean	Median	Range
a	2.6	1.3	0.8–56.4	2.6	1.6	0.8–16.7	2.5	2	0.9–6.6	3.8	2.8	0.8–16.3
b	10.1	5.9	3.3–140.7	5.4	5	3.3–11.7	9.6	8.7	3.3–25.6	7.7	6.6	3.3–18.3
c	1.8	1.1	0.7–31.3				1.9	1.4	0.7–9.7	2.5	2	0.7–8.9
d	2.2	1.1	0.7–50.8				5.5	4.1	0.7–16.9			
e	1.9	1.1	0.7–39.2				4.1	1.8	0.7–17.1			
f	1.8	1	0.7–58.5				1.7	1.7	0.8–4.2	2.4	1.9	0.7–14.9
g				3.6	2.9	1.7–11.0				5	4.1	1.7–17.2
i	1.8	1	0.7–60.4	1.2	0.9	0.7–3.4				2.3	1.5	0.7–13.9
	Interior Melilite (GOS)			**Rim Melilite (GOS)**			**Interior Spinel (GOS)**			**Rim Spinel (GOS)**		
	Mean	Median	Range	Mean	Median	Range	Mean	Median	Range	Mean	Median	Range
a	1.9	1.03	0.2–12.9	1	0.7	0.2–7.7	0.7	0.5	0.2–1.8	1.3	0.8	0.2–9.0
b	2.7	1.8	0.3–14.4	0.8	0.6	0.3–3.50	1.2	0.7	0.2–13.4	0.9	0.5	0.2–5.8
c	2	1.4	0.4–14.9				1.7	0.8	0.4–8.0	1.2	0.7	0.4–7.3
d	1.8	1.1	0.2–14.6				0.8	0.8	0.3–2.18			
e	1.8	1.3	0.3–13.1				1.7	0.9	0.4–1.3			
f	1.4	1	0.2–13.9				0.7	0.5	0.3–2.2	1.4	0.8	0.3–8.6
g				1.3	1	0.2–6.5				0.7	0.5	0.1–6.2
i	1.4	0.9	0.2–8.0	1	0.8	0.3–3.8				1	0.7	0.3–5.6
	Interior Melilite (GAM)			**Rim Melilite (GAM)**			**Interior Spinel (GAM)**			**Rim Spinel (GAM)**		
	Mean	Median	Range	Mean	Median	Range	Mean	Median	Range	Mean	Median	Range
a	0.8	0.8	0.2–2.7	0.6	0.5	0.2–2.3	0.4	0.4	0.2–0.8	0.5	0.5	0.9–1.6
b	1	0.9	0.4–2.8	0.7	0.6	0.3–1.8	0.5	0.4	0.2–1.7	0.5	0.4	0.2–1.6
c	1	0.9	0.4–2.6				0.7	0.6	0.4–2.5	0.6	0.5	0.3–1.0
d	0.8	0.8	0.2–3.9				0.5	0.4	0.3–1.5			
e	0.9	0.9	0.3–2.7				0.7	0.7	0.3–1.3			
f	0.9	0.8	0.3–2.4				0.4	0.4	0.3–0.6	0.7	0.6	0.3–1.6
g				0.8	0.7	0.3–1.8				0.4	0.4	0.1–1.6
i	0.8	0.7	0.2–2.6	0.8	0.7	0.3–4.4				0.6	0.5	0.2–3.4

Table 2
Deformation parameters and grain sizes for melilite and spinel grains in Hedgehog, determined using EBSD data. GOS: Grain orientation spread in degrees, GAM: Grain average misorientation in degrees.

	Spinel		Melilite	
	Interior	Rim	Interior	Rim
Grain size (μm) Range	0.7 to 25.6	0.7 to 18.3	0.7 to 140.7	0.8 to 16.6
$Grain\ size_{mean}$ (μm)	6.7	4.3	2.8	3.4
$Grain\ size_{median}$ (μm)	5.2	3.2	1.2	2.7
GOS_{mean}	1.19	1.14	1.96	1.17
GOS_{median}	0.71	0.63	1.19	0.81
GAM_{mean}	0.52	0.52	0.90	0.68
GAM_{median}	0.46	0.46	0.86	0.63

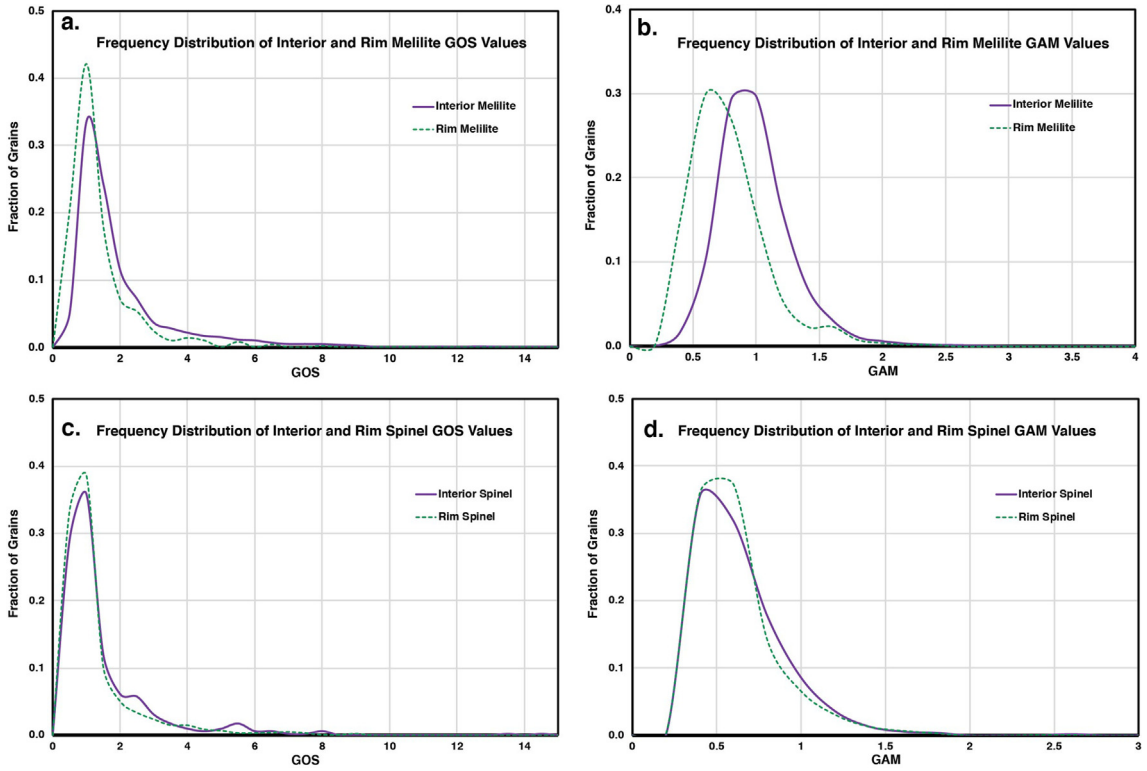

Fig. 7. (a) Frequency distribution of GOS values of interior and rim melilite. (b). Frequency distribution of GOS values of interior and rim spinel. (c) Frequency distribution of GAM values of interior and rim melilite. (d) Frequency distribution of GAM values of interior and rim spinel.

Table 3a
z-Test: Two Sample for Means (Interior and Rim Melilite GOS).

	Interior Melilite GOS	*Rim Melilite GOS*
Mean	1.96	1.17
Known Variance	10.12	1.54
Number of grains	4042	429
Hypothesized Mean Difference	0.00	
z	10.10	
Probablity (P) (Z<=z) one-tail	<0.01	
z Critical one-tail	1.64	
Probablity (P) (Z<=z) two-tail	<0.01	
z Critical two-tail	1.96	

Table 3b
z-Test: Two Sample for Means (Interior and Rim Melilite GAM).

	Interior Melilite GAM	*Rim Melilite GAM*
Mean	0.90	0.68
Known Variance	0.09	0.09
Number of grains	4042	429
Hypothesized Mean Difference	0.00	
z	14.10	
Probablity (P) (Z<=z) one-tail	<0.01	
z Critical one-tail	1.64	
Probablity (P) (Z<=z) two-tail	<0.01	
z Critical two-tail	1.96	

Table 4a
z-Test: Two Sample for Means (Interior and Rim Spinel GOS).

	Interior Spinel GOS	*Rim Spinel GOS*
Mean	1.19	1.14
Known Variance	1.93	3.23
Number of grains	450	1006
Hypothesized Mean Difference	0.00	
z	0.61	
Probablity (P) (Z<=z) one-tail	0.27	
z Critical one-tail	1.64	
Probablity (P) (Z<=z) two-tail	0.54	
z Critical two-tail	1.96	

Table 4b
z-Test: Two Sample for Means (Interior and Rim Spinel GAM).

	Variable 1	*Variable 2*
Mean	0.52	0.52
Known Variance	0.06	0.06
Number of grains	450	1006
Hypothesized Mean Difference	0.00	
z	0.19	
Probability (P) (Z<=z) one-tail	0.42	
z Critical one-tail	1.64	
Probability (P) (Z<=z) two-tail	0.85	
z Critical two-tail	1.96	

3.4. Microstructural analysis using TEM

We prepared a FIB section of the interior of Hedgehog and analyzed it using TEM to compare the implications of our EBSD results with previously conducted TEM analyses of CAI melilite and spinel, as well as with experimentally shocked melilite and spinel. The location of the FIB section is shown in Fig. S10. The FIB section extracted from the interior of Hedgehog contains an assemblage of spinel and melilite grains (Fig. 9) with a layer of calcium carbonate (formed during the parent body or terrestrial alteration of the meteorite) between spinel and melilite. EDS maps show that the spinel grains are endmember of $MgAl_2O_4$. The Fourier transforms of HRTEM image regions show that spinel grains are closely oriented with respect to each other. High-resolution TEM shows that the spinel grain also contains fault stacking along the [1 1 1] direction (Fig. 9i, j, and S11). In comparison, EDS maps reveal that melilite has a uniform chemical composition. SAED patterns acquired across the melilite region of the FIB section show that all grains are crystalline, but BF-STEM imaging shows that they contain a high density of dislocations (Fig. 9g, h). We calculated a dislocation density of $\sim 4.4 \times 10^9$ cm^{-2} (Fig. S12) for an oriented melilite grain.

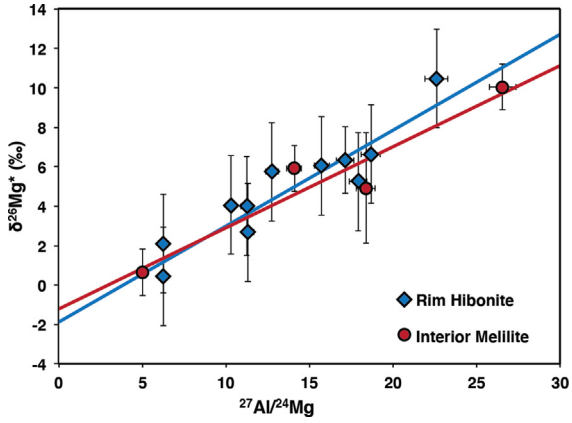

Fig. 8. ^{26}Al-^{26}Mg systematics in Hedgehog interior and rim. The interior defines the slope (^{26}Al/^{27}Al ratio) = $(6.1 \pm 1.8) \times 10^{-5}$ and intercept $(\delta^{26}Mg^*)_0 = -1.4 \pm 2.0‰$ (MSWD = 1.2). The rim defines the slope (^{26}Al/^{27}Al ratio) = $(6.7 \pm 1.6) \times 10^{-5}$ and intercept $(\delta^{26}Mg^*)_0 = -1.6 \pm 1.6‰$ (MSWD = 1.0). The errors shown here are 2σ.

4. DISCUSSION

The microstructures observed in the melilite and spinel suggest that Hedgehog experienced severe deformation.

Table 5
^{26}Al-^{26}Mg Systematics of Hedgehog.

	^{27}Al/^{24}Mg	2σ	δ^{25}Mg	2σ	δ^{26}Mg*	2σ
Interior Melilite-A	26.6	0.1	−0.4	1.4	10.2	2.7
Interior Melilite-B	14.1	0.1	3.5	1.1	6.1	2.0
Interior Melilite-C	5.1	0.1	1.5	0.9	0.7	1.4
Interior Melilite-D	18.4	0.1	9.8	1.6	5.4	3.0
Rim Hibonite-A	22.6	0.2	5.1	1.9	10.8	2.6
Rim Hibonite-B	11.3	0.2	1.7	1.8	2.8	2.0
Rim Hibonite-C	10.3	0.2	0.3	1.7	4.2	1.9
Rim Hibonite-D	6.3	0.2	1.5	1.7	2.1	1.7
Rim Hibonite-E	6.3	0.2	1.7	1.7	0.4	1.6
Rim Hibonite-F	11.2	0.2	0.5	1.8	4.1	2.0
Rim Hibonite-G	12.8	0.2	2.4	2.0	5.9	2.8
Rim Hibonite-H	17.9	0.2	1.9	1.9	5.4	2.4
Rim Hibonite-I	15.8	0.2	8.9	1.7	6.3	1.7
Rim Hibonite-J	18.7	0.2	8.4	1.7	6.9	1.7
Rim Hibonite-K	17.1	0.1	−4.1	1.3	6.2	1.4

Melilite records relatively intense deformation in the interior compared to the WL rims, however, spinel does not show a significant difference in the deformation metrics in the interior and the rim. In this section, we compare these microstructures with previous studies and discuss possible explanations, including shock deformation in the nebula or meteoritic body, and collisions in the disk.

4.1. Effect of grain size on deformation metrics

EBSD analysis of olivine in various ordinary chondrites shows that the GOS can be affected by grain size, specifically, the mean GOS values were found to be consistently higher for coarser olivine grains (Ruzicka and Hugo, 2018). Therefore, grain size and possibly other factors such as differences in mineral composition, grain orientation, orientation of grain boundaries, and rock and mineral anisotropy in interior and rim melilite could have an important effect on the deformation metrics, i.e., GOS and GAM. Compositionally, mineral phases from the interior of Hedgehog are similar to the rim phases, with only minor variations (Table S1). Additionally, we did not observe rock and mineral anisotropy or preferred orientation in mineral phases of Hedgehog. However, there is a significant difference in the grain sizes in some of these phases. The interior melilite grain sizes range from 0.7 to 140 μm with an average of 2.8 μm, whereas rim melilite grain sizes range from 0.7 to 16.6 μm with an average of 3.4 μm. The variation in grain size is less pronounced in the spinel, where the interior spinel grain size ranges from 0.7 to 25.6 μm with an average grain size of 6.3 μm, and the rim spinel grain size ranges from 0.7 to 18.3 μm with an average grain size of 4.3 μm.

The interior melilite data shows that the deformation parameter GOS does not correlate with grain size, however, GAM may have some correlation with grain size (Figs. S13a, b). To determine the effects of grain size on the deformation metrics used for this study, we re-evaluated the GOS and GAM for rim and interior phases of the same grain size range. Table 6 shows GOS and GAM values for grain size <15 μm for spinel and melilite. The mean GOS value for interior melilite with grain size <15 μm (1.84) is higher than the rim melilite with grain size <15 μm (1.16). The mean GAM value for interior melilite with grain size <15 μm (0.90) is higher than that of the rim melilite with grain size <15 μm (0.68). The mean GOS value of the interior spinel with grain size <15 μm (1.11) is similar to the rim spinel with grain size <15 μm (1.13). Similarly, the mean GAM value for the interior spinel with grain size <15 μm (0.53) is similar to that of the rim spinel with grain size <15 μm (0.52). We applied the two-sample z test to melilite grains <15 μm. For interior and rim melilite grains, the probability (p) of the GOS and GAM values having the same mean is <0.01 (Table 7a, b). Therefore, the interior melilites (with grain size <15 μm) record a much more intense deformation compared to the rim melilites, as seen in their GOS and GAM values. The EBSD data suggest that the interior melilite was strongly deformed before the WL rims formed around it. The CAI then later experienced a milder event that deformed the rim melilite and spinel.

Shock deformation can cause the microstructural deformation seen in Hedgehog. Effects of shock are extremely heterogeneous at the scale of a few microns, causing large local variations in temperature and pressure (Bland et al., 2014). Additionally, the effects of shock deformation are heterogeneous due to the constructive and destructive interferences of shock waves and heterogeneity of the medium. The region where shock waves interfere constructively would record higher deformation as observed in GOS and GAM because overlapping shockwaves would combine to produce localized regions of higher peak pressures. Similarly, the regions of destructive interference of shock waves would cause regions of low deformation. If Hedgehog was a spherically symmetric inclusion deformed during a shock event after its rim formation, it is possible that constructive interference of shock waves could selectively cause stronger deformation in the interior. As the entire Hedgehog CAI was not mapped by EBSD, it is not possible to completely exclude the possibility that constructive and destructive

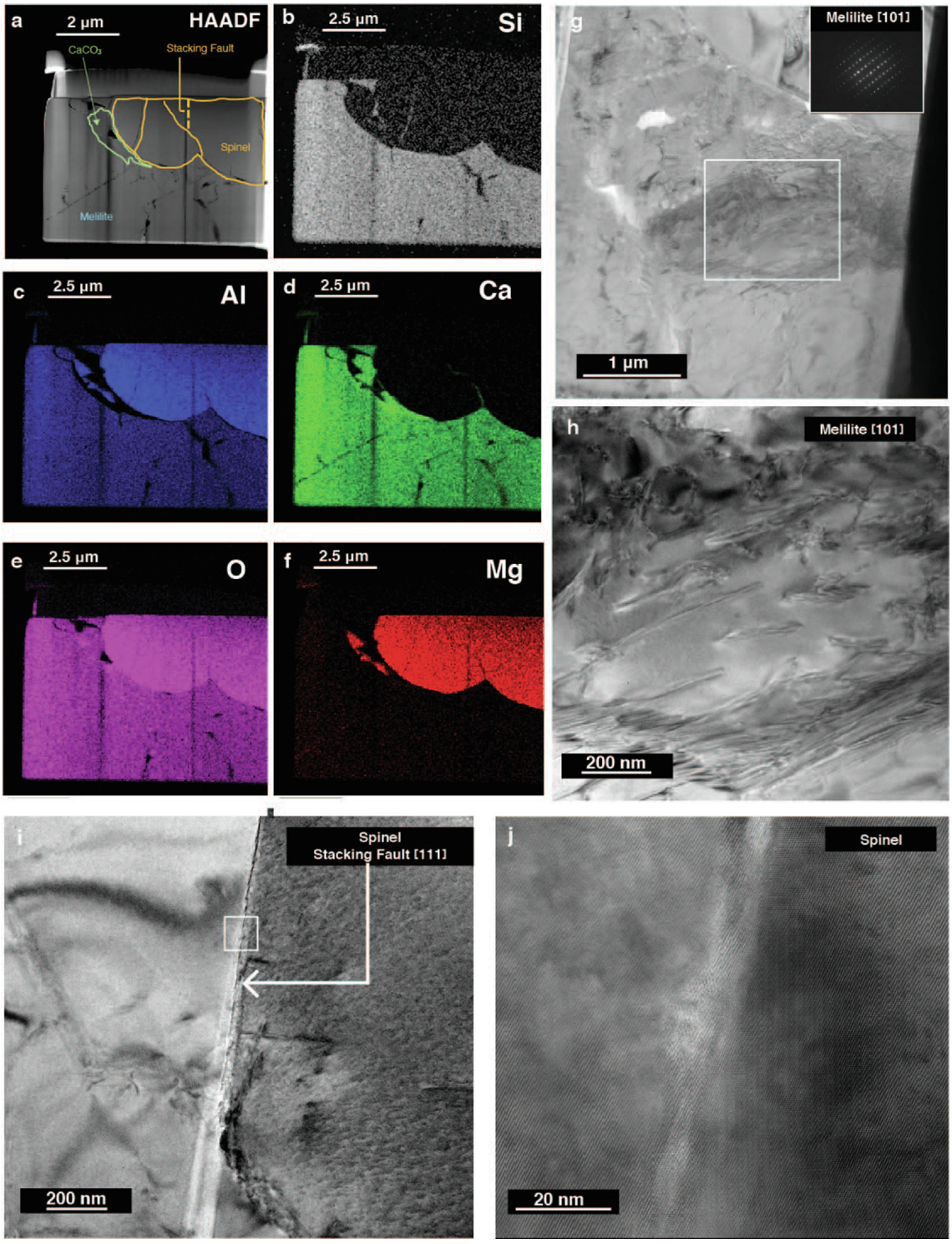

Fig. 9. FIB and TEM data on Hedgehog. (a) High-angle annular-dark-field image of the FIB section. (b–f) EDS maps of the FIB section showing distribution of Si, Al, Ca, O, and Mg. (g) Bright field image of the oriented melilite grain. SAED pattern of the oriented melilite is shown as an inset. (h) Higher-magnification bright-field image of local area of oriented melilite (white box from Fig. g) that shows dislocations in the grain. (i). Bright field image of the spinel grain with a stacking fault. (j) High-resolution image of the stacking fault (white box from Fig. I; also see Supplementary Material).

Please cite this article in press as: Mane P., et al. Earliest evidence of nebular shock waves recorded in a calcium-aluminum-rich Inclusion. *Geochim. Cosmochim. Acta* (2022), https://doi.org/10.1016/j.gca.2022.06.006

Table 6
Deformation parameters and grain sizes for melilite and spinel grains (grain size <15 μm) in Hedgehog, determined using EBSD data. GOS: Grain orientation spread in degrees, GAM: Grain average misorientation in degrees.

	Spinel (grain size <15 μm)		Melilite (grain size <15 μm)	
	Interior	Rim	Interior	Rim
$Grain\ size_{mean}$ (μm)	5.5	4.1	2.0	3.4
$Grain\ size_{median}$ (μm)	4.6	3.2	1.15	2.7
GOS_{mean}	1.11	1.13	1.84	1.16
GOS_{median}	0.66	0.63	1.17	0.81
GAM_{mean}	0.53	0.52	0.90	0.68
GAM_{median}	0.46	0.46	0.86	0.63

Table 7a
z-Test: Two Sample for Means (Interior and Rim Melilite GOS for grains <15 μm).

	Interior Melilite GOS	*Rim Melilite GOS*
Mean	1.84	1.16
Known Variance	8.28	1.45
Number of grains	3937	428
Hypothesized Mean Difference	0.00	
z	9.21	
Probability (P) (Z<=z) one-tail	<0.01	
z Critical one-tail	1.64	
Probability (P) (Z<=z) two-tail	<0.01	
z Critical two-tail	1.96	

Table 7b
z-Test: Two Sample for Means (Interior and Rim Melilite GAM for grains <15 μm).

	Interior Melilite GAM	*Rim Melilite GAM*
Mean	0.90	0.68
Known Variance	0.09	0.09
Number of grains	3937	428
Hypothesized Mean Difference	0.00	
z	14.21	
Probability (P) (Z<=z) one-tail	<0.01	
z Critical one-tail	1.64	
Probability (P) (Z<=z) two-tail	<0.01	
z Critical two-tail	1.96	

interference of shock waves played a role in generating the observed difference in interior and rim deformation; however, we find this unlikely because such constructive interference would not be limited selectively to the interior region as Hedgehog has an irregular and complex shape. However, such constructive and destructive interference of shock waves would record heterogeneous deformation in both the interior and rim of the CAI, consistent with the large variance observed in GOS and GAM values. We analyzed rims in 4 different maps, and they show consistently low mean and median values for GOS and GAM compared to the interior melilites. For maps a, b, and i, both interior and rim melilites were measured, and the rim melilites show lower mean and median GOS and GAM values compared to the interior melilite as reported in Table 1. Therefore, the overall difference in the interior and the rims is not caused by an artifact of spatial variability and is also unlikely to be due to constructive and destructive interference of shock waves.

4.2. Comparison of EBSD analysis of Hedgehog with microstructural analyses of CAIs using TEM and shock recovery experiments in melilite and spinel

Although there are very few EBSD studies on CAIs (e.g., Bolser et al., 2016; Daly et al., 2017), there are some analyses of their microstructures using TEM (Müller and Wlotzka, 1982; Barber et al., 1984; Greshake et al., 1998). Many of the TEM studies show records of deformation in melilite and spinel in highly localized sections of the CAIs, in the form of high dislocation densities. In addition, shock experiments were performed on melilite (Åk27) at pressures ranging from 11 to 50 GPa (Schäfer et al., 1984). TEM analysis of the shocked melilite showed the presence of abundant dislocations such as stacking faults, amorphous lamellae with a width on the order of the unit-cell dimensions, and the presence of amorphous regions/diaplectic glass of melilitic composition, but no indication of melting. The shocked melilite also exhibits many planar fractures,

Please cite this article in press as: Mane P., et al. Earliest evidence of nebular shock waves recorded in a calcium-aluminum-rich Inclusion. *Geochim. Cosmochim. Acta* (2022), https://doi.org/10.1016/j.gca.2022.06.006

orientated roughly parallel to {0 0 1}, {hk0}, and {*hkl*} directions (Schäfer et al., 1984). Similarly, shock-recovery experiments on spinels were conducted at pressures ranging from 25.5 to 50.5 GPa (Schäfer et al., 1983). It is difficult to see strain features in spinels using optical microscopy, because of their isotropic nature. However, some TEM studies have reported dislocations in some grains and slip locations with a Burgers vector 1/2 ⟨1 1 0⟩ and twin lamellae of the twin law {1 1 1}. Many of the spinel grains show presence of 5 to 500 nm thick {1 1 1} twin lamellae (Schäfer et al., 1983). That Hedgehog melilite shows a high degree of deformation in the EBSD data (Figs. 4–5, S1-S7) and TEM data (Figs. 9, S12) indicates that it experienced significant strain. Further, in comparison to the shock-recovery experiments, the absence of amorphous lamellae in the Hedgehog melilite suggests that the CAI was at an elevated ambient temperature (>∼1000 °C but not high enough to melt the melilite) when it was shocked (Schäfer et al., 1984), preventing a sudden drastic drop in the temperature, and therefore, formation of amorphous regions in melilite. Similarly, the high ambient temperatures also prevented formation of twin lamellae in spinel during the shock event. We note that similar observations were made with the previous TEM analyses of CAIs (Müller and Wlotzka, 1982; Barber et al., 1984; Greshake et al., 1998). It may be possible to record microstructures seen in Hedgehog melilite and spinel at lower peak pressures (<11 GPa) than observed in shock recovery experiments by Schäfer et al., (1983, 1984) in colder ambient temperatures. However, the high dislocation density observed in Hedgehog melilite (∼4.4 × 10^9 cm^{-2}) appears to argue otherwise. For comparison, Schäfer et al. (1984) reported dislocation densities in experimentally shocked terrestrial melilite. The average dislocation densities in melilite shocked to 20–35 GPa are comparable i.e., (7–10) × 10^9 cm^{-2}. Additionally, similar high dislocation densities of up to 3 × 10^{11} cm^{-2} were observed in melilite from CV3 CAIs (Greshake et al., 1998). Therefore, deformation features observed in Hedgehog melilite, and spinel were likely acquired during a shock event at elevated ambient temperatures. Some of the rim melilites show triple junctions, suggesting post-formation annealing, consistent with the elevated high ambient temperatures. At these elevated temperatures, lower peak pressures may be required to produce the dislocation densities observed in melilite, compared with those seen in the shock recovery experiments conducted at room temperature. Alternatively, if the elevated ambient temperatures partially annealed some dislocations, then the initial dislocation density of melilite may have been higher than ∼4.4 × 10^9 cm^{-2}, suggesting higher peak pressures. The peak pressure and temperature estimates of the shock event that deformed Hedgehog are based on limited data and are therefore speculative.

The overall lower GOS and GAM values in the rim melilite compared to the interior melilite suggest that the interior melilite experienced more extensive deformation than its rim (Fig. 7a, b). The average GOS and GAM values of the interior spinel are slightly higher than the rim spinel (Table 2). However, GOS and GAM values of the interior and rim spinel do not show a statistically significant difference (Fig. 7c, d, Table 4). Comparison between the shock behavior of spinel and melilite was not, to our knowledge, evaluated experimentally. However, spinel is harder and presumably more brittle than melilite (spinel has a Mohs hardness of 8 compared to 5.5 for melilite). Similarly, Young's modulus for spinel varies between 182 and 212 GPa (Kushwaha, 2010), whereas that of synthetic gehlenite is 108 ± 6.8 GPa (Jia and Kriven, 2007). These properties suggest that spinel has a higher mechanical strength than melilite. Additionally, differences in the annealing properties of spinel and melilite could be responsible for these minerals recording the effects of shock deformation differently. Alternatively, if interior spinel grains enclosed in melilite were shielded from deformation, it is possible that they did not record high GOS values like melilite. Therefore, we infer spinel is more resistant to shock deformation, thus suggesting that melilite may record shock deformation more efficiently than spinel.

4.3. Timing of deformation

Both the interior and the WL rims record a canonical value for the initial $^{26}Al/^{27}Al$ ratio. Considering the lower limit on the slope of the interior isochron, i.e., 4.3 × 10^{-5}, and rim isochron, i.e., 5.1 × 10^{-5}, and comparing these ratios with the canonical $^{26}Al/^{27}Al$ ratio of 5.2 × 10^{-5} (Jacobsen et al., 2008), the data indicate that the interior and WL rims formed contemporaneously within <200,000 years after CAI formation. The relative ages of the WL rims are consistent with previous studies (Simon et al., 2005; Kawasaki et al., 2012, 2017; Han et al., 2020), indicating that these rims formed soon after the interior at the very beginning of the Solar System. As the interior melilite grains of Hedgehog are significantly more deformed than those in the WL rims, our data suggest that the first deformation event occurred prior to the formation of the rims. Therefore, the mechanism(s) that caused the deformation of the interior melilite was active early, occurring within the first few hundred thousand years of Solar System history.

4.4. Mechanisms of deformation

The microstructural and chronological data presented here provide the following constraints on the processes responsible for the deformation of melilite and spinel in Hedgehog. First, the interior melilite records a more intense deformation compared to the WL rim melilite, suggesting that the process was active before the rim formation. The ^{26}Al-^{26}Mg chronology provides the relative age of the WL rim sequence of ≤200,000 years after CAI formation. Therefore, the process responsible for the deformation of interior melilite and spinel was active ≤200,0000 years after CAI formation. Second, the microstructures in melilite and spinel suggest that this deformation event occurred at a high ambient temperature of >∼1000 °C. However, deformation did not occur at temperatures higher than the melting point of melilite (∼1385 °C) (Deer et al., 1997), because at such higher temperatures melilite and spinel would recrystallize, and deformation signatures would be erased.

Crystallographic deformation can result from several processes such as shock waves, rapid crystallization, and collisions. As observed in the starting materials used for shock-recovery experiments, naturally occurring terrestrial melilite was reported to be almost free of crystallographic defects (Schäfer et al., 1984). Additionally, Hedgehog is a transitional fluffy type A-compact type A, that may have experienced partial melting. The reverse-zoned melilite seen in Hedgehog, usually observed in fluffy type As, is thought to be a product of direct condensation from the decrease in pressure of a hot nebular gas (MacPherson and Grossman, 1984). However, the normal zoning in melilite would suggest recrystallization from a melt. All melilite grains in the interior of Hedgehog are deformed. Thus, the deformation we observe in Hedgehog melilite is not a result of rapid crystallization, but it must have occurred after the crystallization, i.e., below the eutectic temperature. Astrophysical mechanisms such as FU Orionis outbursts, Exor outbursts, and X-ray flares, have been suggested to explain the melting of igneous CAIs and chondrules. However, these mechanisms operate on timescales of months to 10^3-10^5years (Connolly et al., 2006). Therefore, such energetic astrophysical events are inconsistent with the thermal histories of CAIs and chondrules (Connolly et al., 2006). We consider here three processes that could lead to the deformation in the interior of Hedgehog: (1) collision of the CAI with other particles in the protoplanetary disk; (2) impacts on the asteroid parent body hosting Hedgehog; and (3) a shock wave propagating through a region of the disk where CAIs existed as freely floating objects. The early solar nebula was a dynamic environment where grain-to-grain collisions were common, e.g., as evidenced by the presence of compound CAIs (Aléon et al., 2018) and chondrules (Wasson et al., 1995). Thus, a collision of Hedgehog with another object (before the formation of the WL rim), and hence, the deformation of the interior melilite, is conceivable. Grain-to-grain collision was suggested as a mechanism to explain deformation in presolar grains, e.g., stacking defects in presolar spinel (Zega et al., 2014). Numerical simulations of grain interactions in the warm interstellar medium (temperature $\sim 10^4$ K) suggest that grain-to-grain collisions of grains with diameters >30 nm and comprised of individual minerals like silicate, graphite, and diamond result in shattering and fragmentation (Jones et al., 1994). Compared to the individual mineral grains in such simulations, CAIs are larger (mm to cm-sized) and composed of compact aggregates of different mineral components with varied orientations, grain boundaries, mechanical strengths, and weaknesses along cleavage planes. Therefore, a collision of particles would more likely result in either bouncing off each other (Morbidelli and Raymond, 2016) or shattering and fragmentation (depending on the impact velocity) rather than causing the deformation observed in Hedgehog. Additionally, deformation in such a scenario would be directional, i.e., intense deformation at the point of contact, that would diminish radially away from the point of contact in the CAI. However, the average GOS and GAM values in different maps are similar (Table 1), suggesting there is no spatial variation in the deformation parameters in this CAI. Also, a foreign object impacting the CAI would be expected to leave some chemical or morphological trace of itself (such as a crater) inside the CAI, unless the impacting object was another CAI with similar mineralogy. Given that the mineralogy of Hedgehog, a type-A CAI, is consistent with thermodynamic predictions (Simon et al., 1999) and that we do not see chemical or morphological signatures of grain-to-grain collision in the two-dimensional section of Hedgehog, it is less likely that the deformation observed in melilite is due to grain-to-grain collision.

The second possible mechanism of this deformation could be the impacts on the meteoritic parent body that hosted Hedgehog. Impacts were proposed to explain the lineations and petrofabric alignments observed in some carbonaceous chondrites (Bland et al., 2014). In such a scenario, one would expect both the interior and rim materials to be deformed with significant heterogeneity in GOS and GAM values. Additionally, due to impact processes on chondritic parent bodies, the edges of solid chondritic components such as CAIs and chondrules would experience higher temperatures and pressures than their cores, and therefore would be expected to be more deformed (Bland et al., 2014; Forman et al., 2016). However, the EBSD data show clear evidence that the interior melilite in Hedgehog is much more deformed than the rim. Further, microstructural features observed in the CAI are consistent with deformation at a high ambient temperature (>∼1000 °C), which is much higher than the temperatures on the CR2 parent body (50 to 200 °C; Schrader et al., 2008). Additionally, the ^{26}Al-^{26}Mg chronology of Hedgehog and its rims suggests that the first shock event occurred within a few hundred thousand years after the CAI formation, which is before the accretion of the CR2 parent body (3.5 ± 0.5 Ma after CAI formation) (Sugiura and Fujiya, 2014). Therefore, we infer that this deformation observed in Hedgehog is a result of a nebular process and is not related to processes on its parent body.

Shock waves were proposed to explain the melting of chondrules (Desch et al., 2012 and references therein), suggesting that shock was a common phenomenon in the chondrule-forming region. Shock-related deformation was previously reported in CAIs. For example, TEM analysis of several type-A and type-B CAIs show high dislocation densities, deformation lamellae, and low-angle grain boundaries in melilite, suggesting considerable strain (Barber et al., 1984). Further, in many of these CAIs, some spinel grains also contain dislocations (Müller and Wlotzka, 1982), indicating that the spinel was deformed as well. Comparing the Hedgehog EBSD and TEM data with the shock-recovery experiments on synthetic melilite and spinel show that certain microstructures such as amorphous lamellae in melilite and twinning in spinel are absent in Hedgehog. (Schäfer et al., 1983, 1984). High ambient temperature would preclude the formation of amorphous lamellae in melilite and twin lamellae in spinel. Based on results from the previous shock experiments, we suggest that the ambient temperature was between ∼1000 to 1385 °C (Schäfer et al., 1983, 1984).

The intense deformation of the Hedgehog interior and relatively less intense deformation of the WL rims suggest

Please cite this article in press as: Mane P., et al. Earliest evidence of nebular shock waves recorded in a calcium-aluminum-rich Inclusion. *Geochim. Cosmochim. Acta* (2022), https://doi.org/10.1016/j.gca.2022.06.006

that the shock mechanism that caused deformation in melilite was repetitive and was active before its WL rim formed in the CAI-forming region. The dating of CAIs constrains their formation to well within ~1 Ma of the beginning of the Solar System (MacPherson et al., 2012), i.e., at ~4567 Ma (Amelin et al., 2010; Connelly et al., 2012), whereas chondrules formed ~0 to 4 Ma after CAI formation (Villeneuve et al., 2009), i.e., 4567–4563 Ma. Our results, therefore, suggest that while CAIs and chondrules formed in distinct nebular reservoirs that were separated both temporally as well as spatially (<1 au for CAIs versus >2 to 3 au for chondrules), they were nonetheless affected by similar shock processing. These shocks may have also contributed to the compaction of the WL rims around CAIs. Radiometric dating of differentiated meteorites and astrophysical observations in distant protoplanetary disks provide evidence for the rapid formation of planetesimals (within ~1 Ma after CAI formation and close to the star (Kleine and Wadhwa, 2017; Brogan et al., 2015). Such early-formed planetesimals could generate large-scale shocks that would provide a mechanism for the deformation of CAIs. We suggest that nebular shocks are a widespread process in protoplanetary disks.

5. CONCLUSIONS

We analyzed the microstructure of a type-A CAI (Hedgehog) in the NWA 5028 CR2 carbonaceous chondrite using EPMA, EBSD, and TEM. Additionally, we determined the relative timescales of formation of this CAI and its WL rim using ^{26}Al-^{26}Mg age dating. Hedgehog is a transitional fluffy type A- compact type A CAI containing melilite, spinel, perovskite, and opaque metal assemblage in its interior. It is surrounded by a WL rim containing the innermost spinel + hibonite + perovskite layer, middle melilite layer, and outermost pyroxene layer. Both the interior and WL rims of Hedgehog record a canonical ^{26}Al/^{27}Al ratio, suggesting that both the interior and the rim formed within the first ~200,000 years of the early Solar System history. The interior melilite grains show significantly higher deformation compared to the rim melilite. Additionally, deformation microstructures suggest that Hedgehog was deformed at elevated ambient temperatures in the solar protoplanetary disk. We hypothesize that Hedgehog was deformed as a free-floating object soon after the CAI formation at the beginning of the Solar System, by a widespread nebular shock mechanism similar to those responsible for chondrule formation.

Data Availability Statement

Research Data associated with this article is submitted as 'Supplementary Materials'.

Declaration of Competing Interest

The authors declare that they have no known competing financial interests or personal relationships that could have appeared to influence the work reported in this paper.

ACKNOWLEDGEMENTS

This research was supported by the NASA Earth and Space Science Fellowship (NNX13AP41H) to P. Mane, NASA Cosmochemistry (NNX11AK75G PI M. Wadhwa) and NASA Emerging Worlds Programs (NNX15AH41G PI Wadhwa), (NNX15AJ22G and 80NSSC19K0509 PI Zega). We gratefully acknowledge NASA (NNX12AL47G and NNX15AJ22G) and NSF (DMR-1531243) for funding of the instrumentation in the Kuiper Materials Imaging and Characterization Facility at the University of Arizona and NSF facility grant (EAR-1352996) to the SIMS facility at Arizona State University. We would like to thank Center for Meteorite Studies (CMS) at Arizona State University for loaning the NWA 5028 meteorite section. We thank Ken Domanik his help with the EPMA analysis. We thank Alan Boss, Mark Cintala, Harold Connolly, Steve Desch, Emilie Dunham, Timmons Erickson, Scott Messenger, Andrew Needham, Ann Nguyen, Sara Russell, and Stu Weidenschilling for their feedback and helpful discussions about this work. The authors would like to thank the associate editor Hope Ishii and reviewers Andrew Davis, Alex Ruzicka, and Luke Daly for their constructive comments in the review process.

APPENDIX A. SUPPLEMENTARY MATERIAL

Supplementary data to this article can be found online at https://doi.org/10.1016/j.gca.2022.06.006.

REFERENCES

Aléon J., Marin-Carbonne J., McKeegan K. D. and El Goresy A. (2018) O, Mg, and Si isotope distributions in the complex ultrarefractory CAI Efremovka 101.1: Assimilation of ultrarefractory, FUN, and regular CAI precursors. *Geochim. Cosmochim. Acta* **232**, 48–81.

Amelin Y., Kaltenbach A., Iizuka T., Stirling C. H., Ireland T. R., Petaev M. and Jacobsen S. B. (2010) U-Pb chronology of the Solar System's oldest solids with variable ^{238}U/^{235}U. *Earth Planet. Sci. Lett.* **300**, 343–350.

Barber D. J., Martin P. M. and Hutcheon I. D. (1984) The microstructure of minerals in coarse-grained Ca-Al-rich inclusions from the Allende meteorite. *Geochim. Cosmochim. Acta* **48**, 769–783.

Beckett J. R., Live D., Tsay F.-D., Grossman L. and Stolper E. (1988) Ti^{3+} in meteoritic and synthetic hibonite. *Geochim. Cosmochim. Acta* **52**, 1479–1495.

Bland P. A., Alard O., Benedix G. K., Kearsley A. T., Menzies O. N., Watt L. E. and Rogers N. W. (2005) Volatile fractionation in the early solar system and chondrule/matrix complementarity. *Proc. Nat. Acad. Sci.* **102**, 13755–13760.

Bland P. A., Collins G. S., Davison T. M., Abreu N. M., Ciesla F. J., Muxworthy A. R. and Moore J. (2014) Pressure–temperature evolution of primordial solar system solids during impact-induced compaction. *Nat. Commun.* **5**, 1–13.

Bland P. A., Howard L. E., Prior D. J., Wheeler J., Hough R. M. and Dyl K. A. (2011) Earliest rock fabric formed in the Solar System preserved in a chondrule rim. *Nat. Geosci.* **4**, 244–247.

Bollard J., Connelly J. N., Whitehouse M. J., Pringle E. A., Bonal L., Jørgensen J. K., Nordlund Å., Moynier F. and Bizzarro M. (2017) Early formation of planetary building blocks inferred from Pb isotopic ages of chondrules. *Sci. Adv.* **3**, e1700407.

Bolser D., Zega T. J., Asaduzzaman A., Bringuier S., Simon S. B., Grossman L., Thompson M. S. and Domanik K. J. (2016) Microstructural analysis of Wark-Lovering rims in the Allende

and Axtell CV 3 chondrites: Implications for high-temperature nebular processes. *Meteorit. Planet. Sci.* **51**, 743–756.

Brewer L. N., Field D. P. and Merriman C. C. (2009) Mapping and assessing plastic deformation using EBSD. In *Electron backscatter diffraction in materials science, 2nd ed.* (ed. A. J. Schwartz). Springer, pp. 251–262.

Brogan C. L., Pérez L. M., Hunter T. R., Dent W. R. F., Hales A. S., Hills R. E., Corder S., Fomalont E. B., Vlahakis C. and Asaki Y. (2015) The 2014 ALMA long baseline campaign: first results from high angular resolution observations toward the HL Tau region. *Astrophys. J. Lett.* **808**(1), L3.

Catanzaro E. J., Murphy T. J., Garner E. L. and Shields W. R. (1966) Absolute isotopic abundance ratios and atomic weight of magnesium. *J. Res. Natl. Bur. Stand. A Phys. Chem.* **70**, 453.

Connelly J. N., Bizzarro M., Krot A. N., Nordlund Å., Wielandt D. and Ivanova M. A. (2012) The absolute chronology and thermal processing of solids in the solar protoplanetary disk. *Science* **338**, 651–655.

Connolly, Jr, H. C., Desch S. J., Ash R. D. and Jones R. H. (2006) Transient heating events in the protoplanetary nebula. In *MESS II* (eds. D. S. Lauretta and H. Y. McSween). Univ. Arizona Press, Tuscon, pp. 383–397.

Connolly, Jr., H. C. and Jones R. H. (2016) Chondrules: The canonical and noncanonical views. *J. Geophys. Res.: Planets* **121**, 1885–1899.

Daly L., Bland P. A., Saxey D. W., Reddy S. M., Fougerouse D., Rickard W. D. and Forman L. V. (2017) Nebula sulfidation and evidence for migration of "free-floating" refractory metal nuggets revealed by atom probe microscopy. *Geology* **45**(9), 847–850.

Davis A. M., Richter F. M., Mendybaev R. A., Janney P. E., Wadhwa M. and McKeegan K. D. (2015) Isotopic mass fractionation laws for magnesium and their effects on ^{26}Al–^{26}-Mg systematics in solar system materials. *Geochim. Cosmochim. Acta* **158**, 245–261.

Deer W. A., Howie R. A. and Zussman J. (1997) Rock-Forming Minerals: Disilicates and Ring Silicates, vol. 1B. Geological Society of London.

Desch S. J., Morris M. A., Connolly, Jr., H. C. and Boss A. P. (2012) The importance of experiments: Constraints on chondrule formation models. *Meteorit. Planet. Sci.* **47**, 1139–1156.

Ebel D. S. (2006) Condensation of rocky material in astrophysical environments. In *MESS II* (eds. D. S. Lauretta and H. Y. McSween). Univ. Arizona Press, Tuscon, pp. 253–277.

El Goresy A., Nagel K. and Ramdohr P. (1979) Spinel framboids and fremdlinge in Allende inclusions-Possible sequential markers in the early history of the solar system. In *Lunar Planetary Science Conference Proceedings*, pp. 833–850.

Field D. P. (1997) Recent advances in the application of orientation imaging. *Ultramicroscopy* **67**, 1–9.

Forman L. V., Bland P. A., Timms N. E., Collins G. S., Davison T. M., Ciesla F. J., Benedix G. K., Daly L., Trimby P. W., Yang L. and Ringer S. P. (2016) Hidden secrets of deformation: Impact-induced compaction within a CV chondrite. *Earth Planet. Sci. Lett.* **452**, 133–145.

Greshake A., Bischoff A. and Putnis A. (1998) Transmission electron microscope study of compact Type A calcium-aluminum-rich inclusions from CV3 chondrites: Clues to their origin. *Meteorit. Planet. Sci.* **33**, 75–87.

Grossman L. (1975) Petrography and mineral chemistry of Ca-rich inclusions in the Allende meteorite. *Geochim. Cosmochim. Acta* **39**, 433–454.

Grossman L. (1980) Refractory inclusions in the Allende meteorite. *Annu. Rev. Earth Planet. Sci.* **8**(1), 559–608.

Grossman L., Beckett J. R., Fedkin A. V., Simon S. B. and Ciesla F. J. (2008) Redox conditions in the solar nebula: Observational, experimental, and theoretical constraints. *Rev. Mineral. Geochem.* **68**, 93–140.

Han J., Keller L. P., Liu M.-C., Needham A. W., Hertwig A. T., Messenger S. and Simon J. I. (2020) A coordinated microstructural and isotopic study of a Wark-Lovering rim on a Vigarano CAI. *Geochim. Cosmochim. Acta* **269**, 639–660.

Harju E. R., Rubin A. E., Ahn I., Choi B. G., Ziegler K. and Wasson J. T. (2014) Progressive aqueous alteration of CR carbonaceous chondrites. *Geochim. Cosmochim. Acta* **139**, 267–292.

Hezel D. C. and Palme H. (2010) The chemical relationship between chondrules and matrix and the chondrule matrix complementarity. *Earth Planet. Sci. Lett.* **294**, 85–93.

Hezel D. C. and Palme H. (2008) Constraints for chondrule formation from Ca–Al distribution in carbonaceous chondrites. *Earth Planet. Sci. Lett.* **265**, 716–725.

Hood L. L. (1998) Thermal processing of chondrule precursors in planetesimal bow shocks. *Meteorit. Planet. Sci.* **33**, 97–107.

Hood L. L. and Horanyi M. (1991) Gas dynamic heating of chondrule precursor grains in the solar nebula. *Icarus* **93**, 259–269.

Hoppe P., Cohen S. and Meibom A. (2013) Nano SIMS: Technical Aspects and Applications in Cosmochemistry and Biological Geochemistry. *Geostand. Geoanal. Res.* **37**, 111–154.

Hovmöller S. (1992) CRISP: crystallographic image processing on a personal computer. *Ultramicroscopy* **41**, 121–135.

Ito M. and Messenger S. (2010) Thermal metamorphic history of a Ca, Al-rich inclusion constrained by high spatial resolution Mg isotopic measurements with NanoSIMS 50L. *Meteorit. Planet. Sci.* **45**, 583–595.

Jacobsen B., Yin Q., Moynier F., Amelin Y., Krot A. N., Nagashima K., Hutcheon I. D. and Palme H. (2008) ^{26}Al–^{26}-Mg and ^{207}Pb–^{206}Pb systematics of Allende CAIs: canonical solar initial ^{26}Al/^{27}Al ratio reinstated. *Earth Planet. Sci. Lett.* **272**, 353–364.

Jia D. and Kriven W. M. (2007) Sintering behavior of gehlenite, part II. Microstructure and mechanical properties. *J. Am. Ceram. Soc.* **90**, 2766–2770.

Jones A. P., Tielens A., Hollenbach D. J. and McKee C. F. (1994) Grain destruction in shocks in the interstellar medium. *Astrophys. J.* **433**, 797–810.

Kawasaki N., Sakamoto N. and Yurimoto H. (2012) Oxygen isotopic and chemical zoning of melilite crystals in a type A Ca-Al-rich inclusion of Efremovka CV3 chondrite. *Meteorit. Planet. Sci.* **47**(12), 2084–2093.

Kruijer T. S., Burkhardt C., Budde G. and Kleine T. (2017) Age of Jupiter inferred from the distinct genetics and formation times of meteorites. *Proc. Nat. Acad. Sci.* **114**, 6712–6716.

Kawasaki Noriyuk, Itoh Shoich, Sakamoto Naoy and Yurimoto Hisayosh (2017) Chronological study of oxygen isotope composition for the solar protoplanetary disk recorded in a fluffy Type A CAI from Vigarano. *Geochim. Cosmochim. Acta* **201**, 83–102.

Kushwaha A. K. (2010) Vibrational and elastic properties of aluminate spinel $MgAl_2O_4$. *Phys. Rev. B Condens. Matter* **405**, 2795–2798.

MacPherson G. J. and Grossman L. (1984) "Fluffy" Type A Ca-, Al-rich inclusions in the Allende meteorite. *Geochim. Cosmochim. Acta* **48**(1), 29–46.

MacPherson G. J., Kita N. T., Ushikubo T., Bullock E. S. and Davis A. M. (2012) Well-resolved variations in the formation ages for Ca–Al-rich inclusions in the early Solar System. *Earth Planet. Sci. Lett.* **331**, 43–54.

MacPherson G. J., Bullock E. S., Tenner T. J., Nakashima D., Kita N. T., Ivanova M. A., Krot A. N., Petaev M. I. and Jacobsen S. B. (2017) High precision Al–Mg systematics of forsterite-

Please cite this article in press as: Mane P., et al. Earliest evidence of nebular shock waves recorded in a calcium-aluminum-rich Inclusion. *Geochim. Cosmochim. Acta* (2022), https://doi.org/10.1016/j.gca.2022.06.006

bearing Type B CAIs from CV3 chondrites. *Geochim. Cosmochim. Acta* **201**, 65–82.

McKeegan K. D., Kallio A. P. A., Heber V. S., Jarzebinski G., Mao P. H., Coath C. D., Kunihiro T., Wiens R. C., Nordholt J. E. and Moses R. W. (2011) The oxygen isotopic composition of the Sun inferred from captured solar wind. *Science* **332**, 1528–1532.

Merlini M., Gemmi M., Hanfland M. and Crichton W. (2009) High-pressure behavior of akermanite and gehlenite and phase stability of the normal structure in melilites. *Am. Min.* **94**, 704–709.

Morbidelli A. and Raymond S. N. (2016) Challenges in planet formation. *J. Geophys. Res.: Planets* **121**, 1962–1980.

Müller W. F. and Wlotzka F. (1982) Mineralogical study of the Leoville meteorite (CV3): Macroscopic texture and transmission electron microscopic observations. In *Lunar and Planetary Science Conference*, pp. 558–559.

Palme H., Hezel D. C. and Ebel D. S. (2015) The origin of chondrules: Constraints from matrix composition and matrix-chondrule complementarity. *Earth Planet. Sci. Lett.* **411**, 11–19.

Peterson R. C., Lager G. A. and Hitterman R. L. (1991) A time-of-flight neutron powder diffraction study of $MgAl_2O_4$ at temperatures up to 1273 K. *Am. Min.* **76**, 1455–1458.

Richter F. M., Mendybaev R. A. and Davis A. M. (2006) Conditions in the protoplanetary disk as seen by the type B CAIs. *Meteorit. Planet. Sci.* **41**, 83–93.

Ruzicka A. M. and Hugo R. C. (2018) Electron backscatter diffraction (EBSD) study of seven heavily metamorphosed chondrites: Deformation systematics and variations in pre-shock temperature and post-shock annealing. *Geochim. Cosmochim. Acta* **234**, 115–147.

Schäfer H., Müller W. F. and Hornemann U. (1984) Shock effects in melilite. *Phys. Chem. Miner.* **10**, 121–124.

Schäfer H., Müller W. F. and Hornemann U. (1983) Shock effects in $MgAl_2O_4$-spinel. *Phys. Chem. Miner.* **9**, 248–252.

Schrader D. L., Connolly, Jr, H. C. and Lauretta D. S. (2008) Opaque phases in type-II chondrules from CR2 chondrites: Implications for CR parent body formation. *Geochim. Cosmochim. Acta* **72**, 6124–6140.

Simon J. I., Young E. D., Russell S. S., Tonui E. K., Dyl K. A. and Manning C. E. (2005) A short timescale for changing oxygen fugacity in the solar nebula revealed by high-resolution ^{26}Al–^{26}Mg dating of CAI rims. *Earth Planet. Sci. Lett.* **238**, 272–283.

Simon S. B., Davis A. M. and Grossman L. (1999) Origin of compact type A refractory inclusions from CV3 carbonaceous chondrites. *Geochim. Cosmochim. Acta* **63**, 1233–1248.

Simon S. B. and Grossman L. (1997) In situ formation of palisade bodies in calcium, aluminum-rich refractory inclusions. *Meteorit. Planet. Sci.* **32**, 61–70.

Sprinthall R. C. and Fisk S. T. (1990) *Basic statistical analysis*. Prentice Hall Englewood Cliffs, NJ.

Sugiura N. and Fujiya W. (2014) Correlated accretion ages and ε^{54}Cr of meteorite parent bodies and the evolution of the solar nebula. *Meteorit. Planet. Sci.* **49**, 772–787.

Vermeesch P. (2018) IsoplotR: A free and open toolbox for geochronology. *Geosci. Front.* **9**, 1479–1493.

Villeneuve J., Chaussidon M. and Libourel G. (2009) Homogeneous distribution of ^{26}Al in the solar system from the Mg isotopic composition of chondrules. *Science* **325**, 985–988.

Wark D. A. and Lovering J. F. (1977) Marker events in the early evolution of the solar system-Evidence from rims on Ca-Al-rich inclusions in carbonaceous chondrites. In *Lunar and Planetary Science Conference Proceedings*, pp. 95–112.

Wasson J. T., Krot A. N., Lee M. S. and Rubin A. E. (1995) Compound chondrules. *Geochim. Cosmochim. Acta* **59**, 1847–1869.

Weidenschilling S. J., Marzari F. and Hood L. L. (1998) The origin of chondrules at jovian resonances. *Science* **279**, 681–684.

Wood J. A. (1996) Processing of chondritic and planetary material in spiral density waves in the nebula. *Meteorit. Planet. Sci.* **31**, 641–645.

Wright S. I., Nowell M. M. and Field D. P. (2011) A review of strain analysis using electron backscatter diffraction. *Microsc. Microanal* **17**(3), 316–329.

Wright S. I., Nowell M. M., De Kloe R. and Chan L. (2014) Orientation precision of electronbackscatter diffraction measurements near grain boundaries. *Microsc. Microanal.* **20**(3), 852–863.

Wright S. I., Nowell M. M., Lindeman S. P., Camus P. P., De Graef M. and Jackson M. A. (2015) Introduction and comparison of new EBSD post-processing methodologies. *Ultramicroscopy* **159**, 81–94.

Yurimoto H., Krot A. N., Choi B.-G., Aléon J., Kunihiro T. and Brearley A. J. (2008) Oxygen isotopes of chondritic components. *Rev. Mineral. Geochem.* **68**, 141–186.

Zega T. J., Nittler L. R., Busemann H., Hoppe P. and Stroud R. M. (2007) Coordinated isotopic and mineralogic analyses of planetary materials enabled by in situ lift-out with a focused ion beam scanning electron microscope. *Meteorit. Planet. Sci.* **42**, 1373–1386.

Zega T. J., Nittler L. R., Gyngard F., Alexander C. M., Stroud R. M. and Zinner E. K. (2014) A transmission electron microscopy study of presolar spinel. *Geochim. Cosmochim. Acta* **124**, 152–169.

Zolensky M., Nakamura T., Martinez J. and Enokido Y. (2020) An unusual porous, cryptocrystalline forsterite chondrule in Murchison. *Meteorit. Planet. Sci.* **56**(1), 56–60.

Associate editor: Hope Ishii